Marine and Petroleum Geology 133 (2021) 105269

Contents lists available at ScienceDirect

Marine and Petroleum Geology

journal homepage: www.elsevier.com/locate/marpetgeo

Natural tectonic fractures and their formation stages in tight reservoirs of Permian Lucaogou Formation, Jimsar Sag, southern Junggar Basin, NW China

Xiangye Kong [a,b], Jianhui Zeng [a,b,*], Xianfeng Tan [c,**], Kun Ding [d], Qun Luo [e], Qianyou Wang [f], Ming Wen [e], Xin Wang [a,b], Maoyun Wang [a,b]

[a] State Key Laboratory of Petroleum Resources and Prospecting, China University of Petroleum, Beijing, 102249, China
[b] College of Geosciences, China University of Petroleum Beijing, Beijing, 102249, China
[c] College of Petroleum and Gas Engineering, Chongqing University of Science and Technology, Chongqing, 401331, China
[d] China National Petroleum Corp Xinjiang Oil Field, Xinjiang, 834000, China
[e] Unconventional Natural Gas Institute, China University of Petroleum, Beijing, 102249, China
[f] Department of Earth, Ocean and Ecological Sciences, University of Liverpool, Liverpool, L69 3GP, UK

ARTICLE INFO

Keywords:
Tectonic fractures
Formation stages
C–O isotope
Tight reservoirs

ABSTRACT

This study investigates natural tectonic fractures in 22 wells that penetrated the tight oil reservoirs in the middle Permian Lucaogou Formation in the southeastern Junggar Basin, China. Analysis was conducted using conventional image logs of wellbores, acoustic emissions (AEs) data collected from core rock mechanics testing, fluid inclusion analysis, and C–O stable isotopes and Ir element analyses of fracture-filling minerals, in order to constrain the relative timing of fracture development. The geochemical properties of fracture-filling minerals and Kaiser effect points, combined with the regional tectonic analysis, revealed a four-stage fracture development in the tested tight reservoirs. During Stage 1, continuous N–S compression occurred at the end of Late Triassic, producing many NW-trending extensional fractures. Calcite fillings were formed within these fractures at temperatures between 31.7 and 45.0 °C based on fluid inclusion analysis. SW–NE compressive stress was produced in the Middle−Late Jurassic during Stage 2, forming ENE-trending shear fractures. The calcite fillings within these fractures formed at temperatures between 50.1 and 64.6 °C. During Stage 3, intense N–S compression formed NNW-trending shear fractures in the Early Cretaceous, and calcite fillings formed at temperatures between 80.0 and 89.9 °C. Finally, Stage 4 corresponds to nearly N–S compression due to the tectonic activities occurring from Tertiary to nowadays, creating NNW-trending shear fractures; no or minimal partial filling of calcite occurred during this Stage. Based on the relation between the oil generation windows and stages of fracture development, it is proposed that the fractures that developed within the Lucaogou Formation during Stages 2–4 have minimal mineral filling, which is most favorable for oil and gas migration and accumulation.

1. Introduction

Several well-known tight reservoirs are composed of compacted, brittle rocks that have experienced intense diagenetic processes and late-stage tectonism (Sonnenberg and Pramudito, 2009; Rich and Ammerman, 2010; Clarkson et al., 2012; Zou et al., 2012; Nojabaei et al., 2013). The role of fractures in reservoirs in the Jimsar Sag have also been noted. Natural fractures are widespread in tight reservoirs (Nelson, 1985; Laubach, 1988; Lorenz et al., 1989; Gale et al., 2014). In tight rocks, differences in fracture attributes profoundly influence fluid flow and associated oil, gas and water producibility (Laubach, 2003; Cumella and Scheevel, 2008; Olson and Taleghani, 2009). Natural fractures are present in many reservoirs in China, where they are inferred to have a strong effect on the exploration and development potential of potential reservoirs (Zeng and Li, 2009; Li et al., 2017; Singh and Cai, 2018; Kong et al., 2021). Hence, research on fractures in tight reservoirs is critically helpful for assessing the layout of tight oil and gas target zones (Dutton and Hamlin, 1991; Abbasi et al., 2014; Ge et al., 2014; Wang et al.,

* Corresponding author. State Key Laboratory of Petroleum Resources and Prospecting, China University of Petroleum Beijing, Beijing, 102249. China.
** Corresponding author.
E-mail addresses: zengjh@cup.edu.cn (J. Zeng), xianfengtan8299@163.com (X. Tan).

https://doi.org/10.1016/j.marpetgeo.2021.105269
Received 3 October 2020; Received in revised form 24 March 2021; Accepted 2 August 2021
Available online 5 August 2021
0264-8172/© 2021 Elsevier Ltd. All rights reserved.

2016a,b). Tectonic stress is a crucial factor controlling the development, abundance and orientation of fractures in tight reservoirs (Van Golf-Racht, 1982; Hennings et al., 2000; Pearce et al., 2011; Tang et al., 2017; Wang et al., 2018). Matching timing of fractures that developed during different stages of tectonic activity to petroleum generation and expulsion stages can help predict how the fractures control the petroleum-bearing potential of the tight oil and gas reservoirs (Perez and Boles, 2005; Filho and Sepehrnoori, 2017; Zhang et al., 2020a; Cao et al., 2021).

The Permian Lucaogou Formation in the Junggar Basin is one crucial tight sandstone oil target of China (Kuang et al., 2012; Du et al., 2014). Wells from this Formation including J37, J251, and J32, drilled in the Jimsar Sag within the southeastern part of the Basin, have provided economic oil flows since 2010. Excellent source rocks with vitrinite reflectance (Ro value) generally between 0.8 and 1.0 have developed in the Jimsar Sag (Kuang et al., 2012). These source rocks have a relatively high oil generation potential and represent a total resource of 1 billion tons, thus indicating good exploration potential (Carroll and Bohacs, 2001; Xie et al., 2015; Pan et al., 2016).

Since the late Paleozoic, the Jimsar Sag has undergone varying degrees of superposition of multiple stages of tectonic activity (Yang et al., 2004; Zhao and Du, 2012; Si et al., 2013). These tectonic activity stages have not only controlled the stratigraphic relationship and tectonic characteristics within the Jimsar Sag but also produced varying stages of tectonic fractures development, affecting the mechanical properties of tight reservoirs in this Formation (Si et al., 2013). The existing research mainly concentrates on the lithological and sedimentary characteristics, pore structure, and regional tectonics associated with tight oil surveying in the Jimsar Sag (Kuang et al., 2012; Zhang et al., 2014; Jiang et al., 2015; Xi et al., 2015; Qiu et al., 2016). However, less attention has been given to the natural fracture systems in this area. The relationship between natural tectonic fractures, oil and gas movement and gathering, and their influence on development optimization has not yet been established. Hence, the tectonic fractures in the tight oil reservoirs of this Formation must be systematically studied.

2. Geological setting

The Junggar Basin, one major superimposed petroliferous basin in China, is positioned in north of Xinjiang Uyghur Autonomous Region and covers approximately 38 × 10^4 km^2 (Zhao, 1992a, 1992b, 1992b; Chen et al., 2003; Cao, 2005; Cao et al., 2006; Xiao et al., 2010). The basin was formed in late Early Permian, when the Bogda trough on its southern margin started to close and orogeny occurred. The Jimsar Sag connected with the Bogda Piedmont Sag and the Fukang Sag, and a set of volcanic molasses, which was thick in the south and thin in the north, was deposited (He et al., 2013; Zhao et al., 2014; Liang et al., 2016). By the middle Permian, the lacustrine facies of the Lucaogou Formation had deposited as a separate sedimentary unit. Tectonic fractures directly resulted from local tectonism. Tectonism frequently occurred in the Junggar Basin during the Middle Jurassic: three episodes caused intense vibrations, representing the most important reworking stages of the Jimsar Sag (Jiang et al., 2015; Cao et al., 2016; Tao et al., 2016). The Jimsar Sag is a secondary tectonic unit of the eastern uplift of the Basin (Fig. 1A) and lies in the southwest of this uplift. The Jimsar Sag covers approximately 1278 km^2 and is bounded by Fukang fault belt, Jimsar fault, Guxi uplift, and Laozhuang/Xidi faults to the south, north, east and west respectively (Fig. 1B). The Lucaogou Formation spreading throughout the sag is 200–250 m thick on average and is thicker in the south and west. The studied tight reservoirs in the Permian strata of this Formation (P_2l) lie below the Wutonggou Formation (P_3wt) and above the Jiangjunmiao Formation (P_2j).

The Lucaogou Formation is separated vertically into two large sedimentary cycles (Lu-1, Lu-2), each of which is further divided by lithological variations into two members: $P_2l_2^1$ (upper) and $P_2l_2^2$ (lower) of Lu-2, and $P_2l_1^1$ (upper) and $P_2l_1^2$ (lower) of Lu-1 (Fig. 2). Two target zones for petroleum development with basically high petroleum prospect and tight substrate occur in the upper and lower parts of this Formation (Zhang et al., 2017; Cao et al., 2016). The upper and lower target zones lie in member $P_2l_2^2$ of cycle Lu-2 and member $P_2l_1^2$ of cycle Lu-1 respectively. The upper target zone initially developed in the east slope of the sag, with a thickness generally between 13.3 and 43.0 m. The lithology is dominated by gray dolerite, and feldspathic and dolomitic lithic sandstones, interwound with gray and dolomitic mudstones. The sandstone and mudstone beds are rich in carbonate and laterally continuous. The lower target zone is developed across the sag and has a thickness of 7.5–67.5 m; the rock types consist mainly of gray dolomitic siltstone, argillaceous siltstone with limy mudstone, dolomitic mudstone, and minor carbonaceous mudstone (Wu et al., 2016; Liu et al., 2017, 2018). Generally, the lower target zone is dominated by clastic rocks with relatively minor amounts of carbonate.

3. Description of fractures

Outcrop, core, microscopic and image log investigations demonstrate that tectonic fractures generally are well developed in the Lucaogou Formation and can be separated into two basic classes: inclined fractures and bedding-parallel fractures.

3.1. Fracture characteristics observed in field outcrops

Tectonic fractures are commonly seen in outcrops of the Lucaogou Formation. Shear fractures are the most common type of tectonic fractures; they usually occur in an "X" configuration, have stable attitudes, with lengths extending 0.1–5 m. Shear fracture surfaces are generally straight and smooth with striations and en-echelon steps, and the fracture tails form wing cracks or rhombus rings. Extension fractures have variable attitudes, with rough and uneven fracture surfaces. The fracture

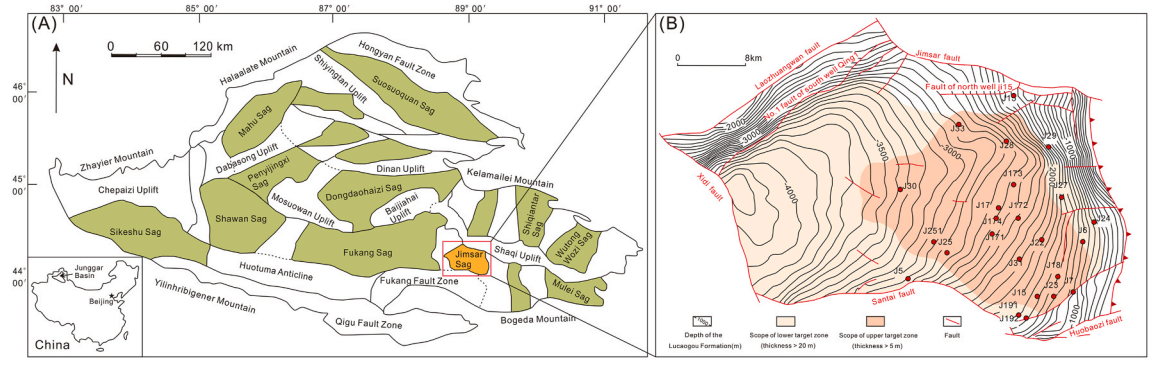

Fig. 1. Location and sketch geological map of the Junggar basin and Jimusar Sag. A: the primary uplifts and sags of the Junggar basin (modified from Qiu et al., 2016); B: the structural map of the top of the Middle Permian Lucaogou Formation of the Jimusar Sag (modified from Qiu et al., 2016).

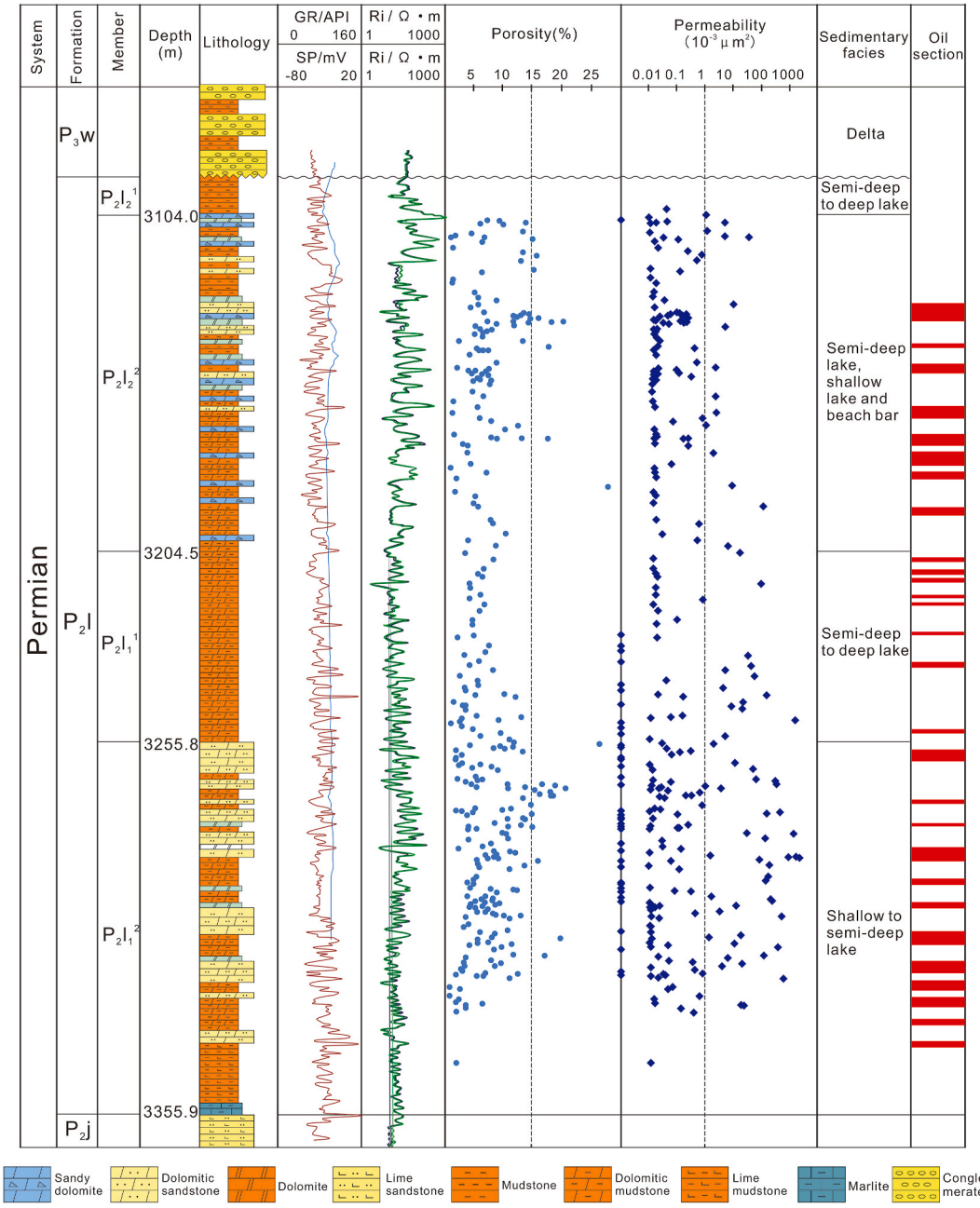

Fig. 2. Comprehensive well logging evaluation chart of the Lucaogou Formation reservoir in the Jimsar Sag (Well J174), modified after Wu et al. (2016) and Kuang et al. (2012). SP—spontaneous potential; GR—gamma ray; Ri—resistivity of intrusion zone; Rt—formation resistivity.

apertures range from 0.1 to 5 mm, and the fractures are dominant non-mineralized to partially-filled (Fig. 3A).

3.2. Core fracture characteristics

Tectonic fractures with lengths between 0.1 cm and 20 cm were recorded in the core data from 22 wells in the study area (Fig. 1B), which include bedding-parallel shear fractures, inclined shear fractures and inclined extension fractures (Fig. 3C and D). Inclined tectonic fractures are mostly discontinuous. The inclined tectonic fractures that cross cut bedding-parallel fractures usually contain hydrocarbon materials; otherwise, they often bear no hydrocarbon materials.

Bedding-parallel fractures are widely developed in the cores, which spread on the bedding surfaces at low angles, or horizontally, and are usually associated with inclined fractures, thereby forming intertwining fracture networks. These networks greatly increase the pore space and seepage capability of the tight reservoirs and provide a pathway for hydrocarbon migration, thereby greatly improving the reservoir properties. Under formation conditions, the aperture of the bedding-parallel fractures are about 0.1–4.5 μm, and bedding-parallel fractures are mostly closed but can become reservoir space if they become filled with hydrocarbons; such fractures are commonly preserved. The fractures unfilled with hydrocarbons commonly become primary pathways for underground fluid migration. During the fluid movement, the temperature and pressure variations enable the fractures to transport substantial amounts of rock-forming materials, which are ultimately oversaturated and precipitated; for example, $CaCO_3$ migrated and formed poikilitic calcite by precipitation and cementation. These precipitated and cemented calcites block the space within the fractures, decreasing the fracture effectiveness (Fig. 3C).

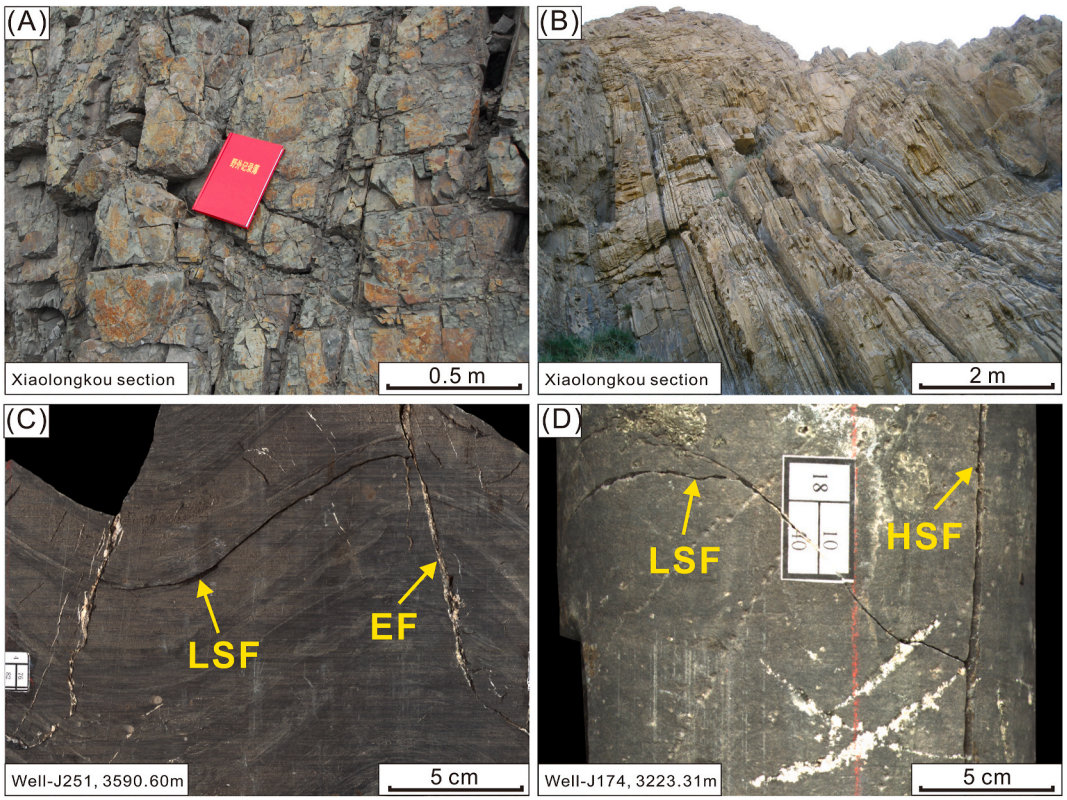

Fig. 3. Photos of fractures in tight oil reservoirs in the middle Permian Lucaogou Formation in the southeastern Junggar Basin: (A) Shear fractures in field outcrops, they usually occur in an "X" configuration, have stable attitudes, and are relatively long, with lengths extending 0.1–5 m and apertures range from 0.1 to 5 mm; (B) Bedding fractures in field outcrops, these bedding fractures are relatively large and are more developed near strata that have a considerable variation in lithology, with lengths extending 1–10 m and apertures range from 0.1 to 0.3 mm; (C) Tectonic fractures in core (Well J251, 3590.60 m); (D) Tectonic fractures in core (Well J174, 3223.31 m). EF-Extension fracture; LSF-Low angle shear fracture; HSF-High angle shear fracture.

3.3. Microscopic fracture characteristics

Common thin sections, thin sections, and scanning electron microscopy (SEM) images were used to conduct observations and analyses. The tectonic fractures cut through laminations or mineral grains and are relatively planar with apertures of 0.1–100 μm and lengths of 0.1–10 mm. The filling degree of these fractures is approximately 70 %, and the coating minerals are mostly calcite and dolomite; although some of the fractures are filled with argillaceous matter (Fig. 4A and B). In dolomitic sandstone and siltstone, microfractures cut through quartz, feldspar, and other minerals, or develop and extend along grain margins (Fig. 4C and D).

The tectonic fractures formed due to minerals cracking under stresses that exceeded the resistance to rupture; tectonic fractures easily form within quartz, feldspar, and other brittle minerals. In contrast, clay minerals have relatively low brittleness, and rarely form tectonic fractures. The tectonic fractures have relatively planar surfaces or zigzagged surfaces, and variable apertures (Fig. 5A and B).

The intergranular fractures more often formed when different minerals are present, but they are undeveloped when same mineral predominates (Fig. 5C and D). Different minerals have differing crystal lattices and growth directions, which enables primary intergranular fractures to form more easily. However, when one mineral predominates, the crystal lattices are consistent, and intergranular fractures form less easily. In addition, when different mineral types are present, their various mechanical properties produce different shape distortions under the same stress; therefore, secondary intergranular fractures form more easily when different minerals are present. The hydrocarbon-generated fractures in these tight reservoirs formed due to hydrocarbon generation when the organic matter (OM) increased in burial depth and reached a certain maturity (Fig. 5E and F). The dissolution pores or cavities formed within the abundant carbonate minerals and then connect with fractures to form pathways for oil and gas storage and migration.

4. Data and methods

84 samples of tight oil reservoirs were collected from 22 exploration wells in the middle Permian Lucaogou Formation in southeastern Junggar Basin, China. These samples were gray dolerite, feldspathic, dolomitic lithic sandstones and dolomitic mudstones. Before the tests, core samples were washed with a mixture of trichloromethane and alcohol to eliminate residual oil, and the samples were then dried at 115 °C for 26 h under vacuum. Each core was drilled to size with a diameter of 2.54 cm and a length of 5.00 cm. All samples were packaged and sent to the laboratory for experimental analysis, which were used in the manufacture of casting thin sections, Fluid inclusions, Ir element measurement, c and O stable isotopes, Acoustic emissions (AEs), scanning electron microscopy (SEM) observation and conventional logging and image logging for fracture identification, and so a uniform sample number was obtained.

4.1. Fluid inclusions

The fluid inclusions were investigated in depth by using microthermometry and laser Raman spectral analyses. With a Linkam THMSG 600 programmable heating-freezing stage installed on a Leica microscope, fluid inclusions were analyzed in the State Key Laboratory of Ore Deposit Geochemistry, Institute of Geochemistry, Chinese Academy of Sciences (CAS). The uncertainty of temperature detection was

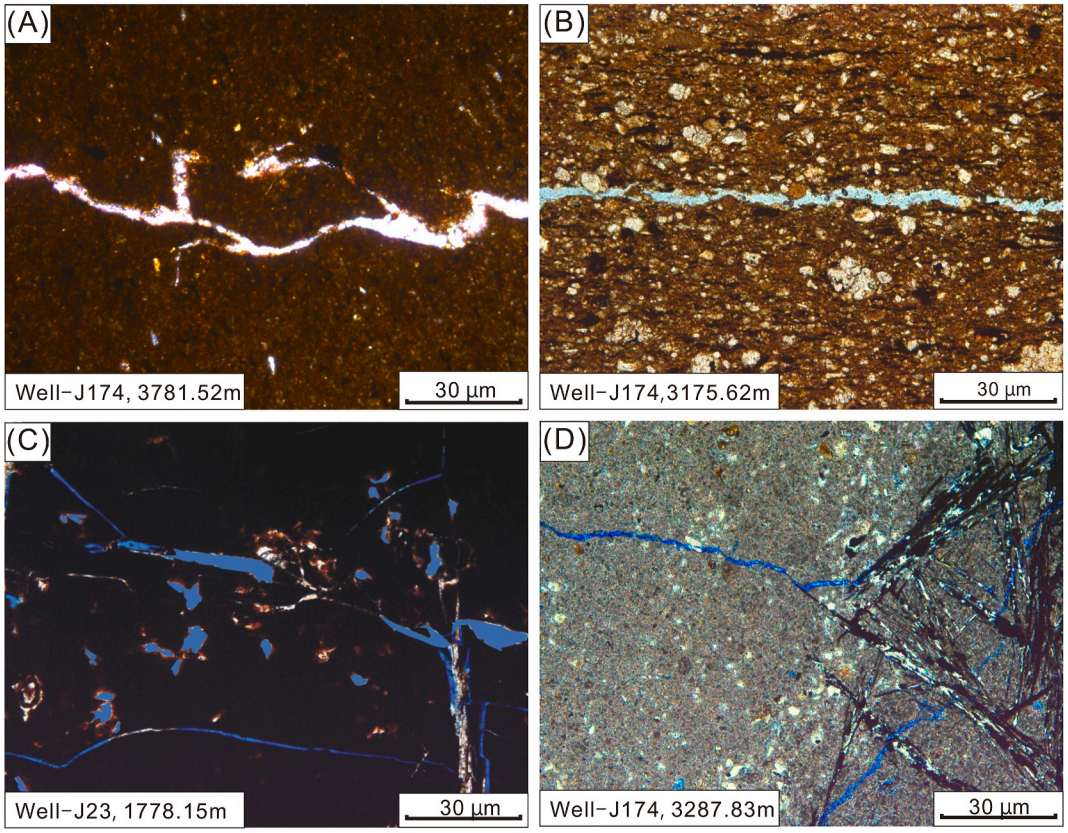

Fig. 4. Photos of microfractures in tight oil reservoirs in the middle Permian Lucaogou Formation in the southeastern Junggar Basin: (A) Tectonic microfracture (Well J174, 3781.52 m); (B) Tectonic microfracture (Well J174, 3175.62 m); (C–D) Thin section from Well J23, 1778.15 m and Well J174, 3287.83 m, showing microfractures cut through quartz, feldspar, and other minerals, or develop and extend along grain margins.

about ±0.2 °C below 50 °C and ±2 °C above 100 °C, and both ice-melting and homogenization temperatures were reached at a heating rate of 0.1 °C/min. Salinity of NaCl–H_2O inclusions was computed using some existing equations (Bodnar, 1993) according to the final ice-melting temperature of dual-phase inclusions. Some individual fluid inclusions were compositionally analyzed by an RM-2000 Laser Raman microprobe at the State Key Laboratory of Geological Processes and Mineral Resources of the China University of Geosciences, Wuhan. The microprobe with an argon ion laser was operated at a laser source of 514 nm and a scanning range of 100–4300 cm^{-1} with 60 s of accumulation for each scan. The laser beam width was about μm, and the spectral resolution was ~0.14 cm^{-1}.

4.2. Ir element measurement

Platinum-group element (PGE) concentrations of whole-rock powders were determined according to Sun et al. (2009) on an Elan6000 ICP–MS meter (Perkin Elmer-Sciex) at Guangzhou Institute of Geochemistry, and an Iso-Probe-T NTI-MS meter (Thermo Scientific) at Institute of Geology and Geophysics. PGE was also detected by a Fe–Ni sulfide fire assay. The powdered samples (each about 10 g) were blended with $Na_2B_4O_7$ (40 g), Fe (2.5 g), Ni (1.0 g) and S (1.0 g) and removed into a fired clay crucible. The above blends were then added with working solutions of ^{185}Re and ^{190}Os spikes, covered with 5 g of $Na_2B_4O_7$ powder and fused at approximately 1050 °C for 45 min (Sun et al., 2009). The resulting beads were put in a glass beaker with 15 ml of H_2O, and then 30 ml of HCl was added. The solutions were heated until being clear and then filtered, and then the insoluble residues were placed into a distilling instrument for Os distillation (Sun et al., 2009). Os concentrations in the resulting Os solutions were measured by isotope dilution. After that, PGE in the remaining solutions was preconcentrated, and Os was all eliminated chemically according to Sun et al. (2009). At last, the volume of the remaining solution was diluted to 10 ml by adding H_2O for analysis of Ru, Rh, Pd, Re, Ir and Pt. The detection limits of these elements were 0.002, 0.0015, 0.025, 0.0007, 0.001 and 0.006 ng/g respectively (Sun et al., 2009).

4.3. C and O stable isotopes

Based on crosscutting relationships, the fillings from three fractures that had different strikes and shapes were selected for C and O stable isotopic analysis. Values of $\delta^{18}O$ were detected for stable isotope ratio mass spectrometry on a GV Iso-Prime II device equipped with a Multi-Prep® online carbonate synthesis instrument at the Guangzhou Institute of Geochemistry, CAS. The sample material (about 0.1 mg) was put into a reaction vessel to react with 102 % H_3PO_4 (specific gravity 1.92 g/cm^3) at 90 ± 1 °C in the Multi-Prep® system. The released CO_2 was harvested, cleaned and removed for mass spectrometry on an online Dual Inlet® system. The O and C isotope compositions were represented as standard δ-notation relative to SMOW and PDB, respectively. GBW04405 (a Chinese state standard) and NBS-19 (a global carbonate standard) were also analyzed. External precision was higher than ±0.1 ‰ (1σ) for both $\delta^{13}C$ and $\delta^{18}O$ detections.

4.4. Acoustic emissions (AEs)

AEs of cores from 7 wells (J30, J32, J174, J015, J5, J251, J15) were tested to investigate the fracture formation stages within the Lucaogou Formation tight oil reservoirs.

Tight brittle rocks in strata that have experienced paleo-tectonic stresses have a stress "memory" (Paul et al., 2015). Microscopic or concealed micro-fractures are widespread in underground rock

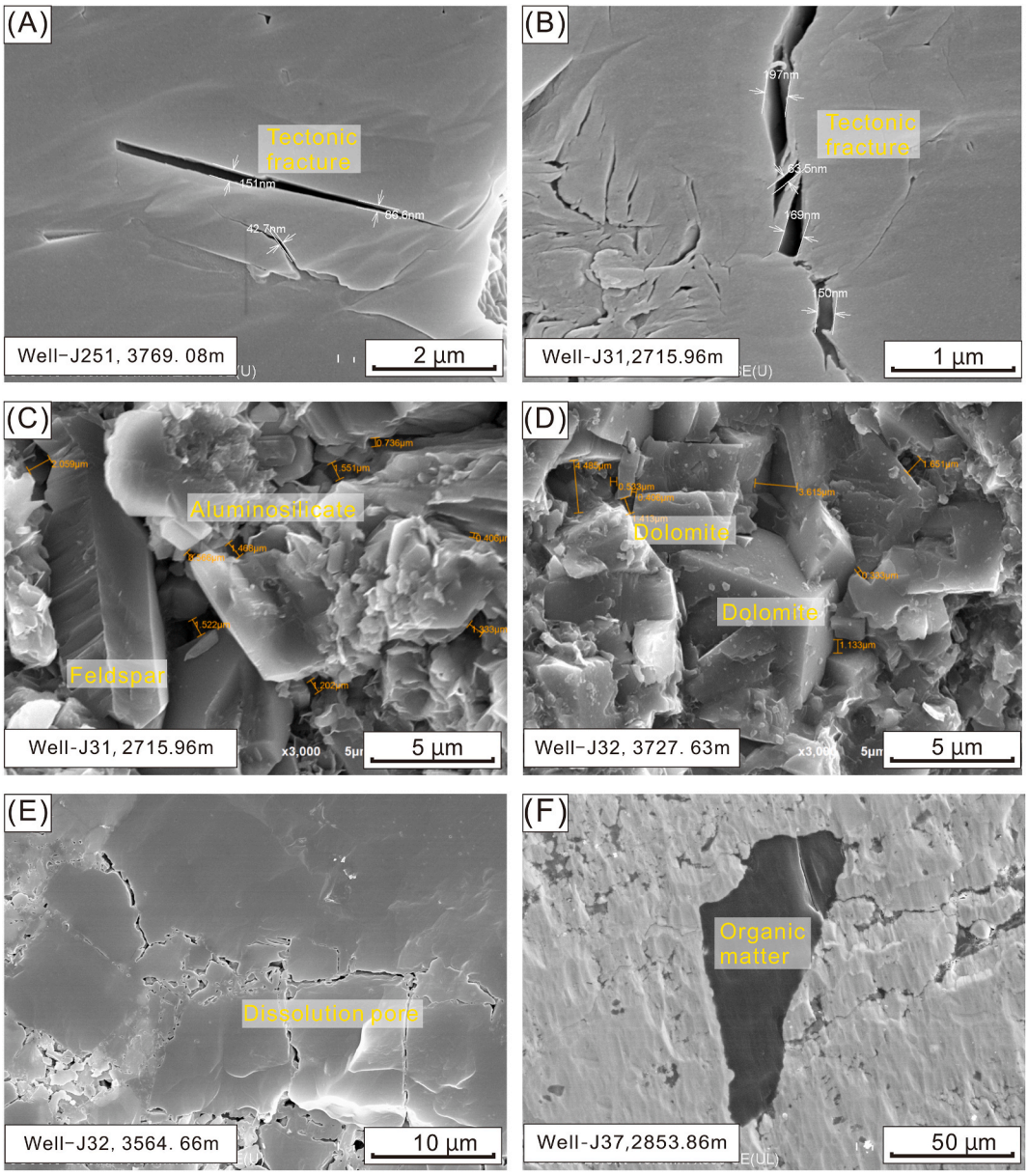

Fig. 5. Scanning electron microscope images of microfractures in tight oil reservoirs in the middle Permian Lucaogou Formation in the southeastern Junggar Basin: (A) Tectonic microfractures (Well J251, 3769.08 m); (B) Tectonic microfractures (Well J31, 2715.96 m); (C) Intergranular fractures (Well J31, 2715.96 m); (D) Intergranular fractures are undeveloped when same mineral predominates; (E) Hydrocarbon-generated fractures (Well J23, 3564.66 m); (F) Hydrocarbon-generated fractures (Well J37, 3253.68 m).

formations, which experienced changes in the tectonic stress field throughout its geologic history. Micro-fractures begin to expand when the applied stress in the laboratory experiment reaches the paleo-strength, which accordingly generates increasing acoustic emission times and strength; therefore, the stress value imposed in the laboratory at a particular point may be equivalent to the strength of the paleo-stress field.

Samples JM122 and JM132 from Well J251, JM34 and JM43 from Well J32, and JM58 and JM69 from Well J174 were selected for the crustal stress experiments. Uniaxial loading was applied to these samples using an RMT-159C rock mechanics tester designed by Institute of Rock and Soil Mechanics, CAS. The AE system adopted an SAEU2S full-waveform channel analyzer, which simultaneously collects and acquires relevant parameters (e.g. amplitude, ring-down count, energy, available value voltage, rise time) in addition to automatically generating various parameter-relation plots. Displacement loading was adopted at a velocity of 2×10^{-3} mm/s, and the AE probe was a resonant SR150M type. In addition, the following were employed: center frequency ranged within 60–400 kHz and was deployed at the sides of the loading test-piece; sampling frequency 5000 Hz; sampling length 2048; parameter interval 50; filter 20–100 k Hz; waveform threshold 40 dB; parameter threshold 40 dB; and preamplifier gain 40 dB. Testing was conducted after establishing AE detecting system parameters. During the test, the loading system and the AE detecting system were started simultaneously, and the two computer systems then collected the required test data. During the test, loading was repeated twice and then re-loaded until samples were destroyed.

4.5. Scanning electron microscopy (SEM)

The core samples were conducted using a HITACHI SU8010 scanning electron microscope. A Merlin scanning electron microscope equipped

with an energy dispersive spectrometer (EDS) was used for the BSE observations, which were performed through the recording of secondary electron images.

4.6. Conventional logging and image logging for fracture identification

Conventional logging can be used to identify fractured intervals (Aguilera, 1976; Zazoun, 2013). Many conventional logging methods exist, and each has a different sensitivity to fractures. The core observations show 16 non-fractured intervals that contain minimal fractures (fracture surface density <1.5 cm/cm^2), and 23 fractured intervals that contain relatively developed fractures (fracture surface density >3 cm/cm^2), and these intervals were selected to study the response characteristics of conventional logging to fracturing (Fig. 6). After obtaining the fracture responses of various logging sequences, seven logging sequences were optimized to obtain conventional logging parameters of these fractured and non-fractured intervals, as shown in Tables 1 and 2. According to the observations, good fracture responses can be obtained using lithological, electrical resistivity, and porosity logs.

Image logging was developed in the 70's and provides direct logging data that are more precise and detailed (Zeng et al., 2010; Khoshbakht et al., 2012; Xiao et al., 2015; Lai et al., 2017). By comparing the image logging data and core analysis results, one can not only determine the fine reservoir sedimentary characteristics but also identify and observe the fractures. Currently, common image logging tools include the resistivity image logs (e.g. FMI) and acoustic image logs (e.g. UBI). This study mainly employed FMI data to analyze fracture distribution in the tested Formation (Fig. 7).

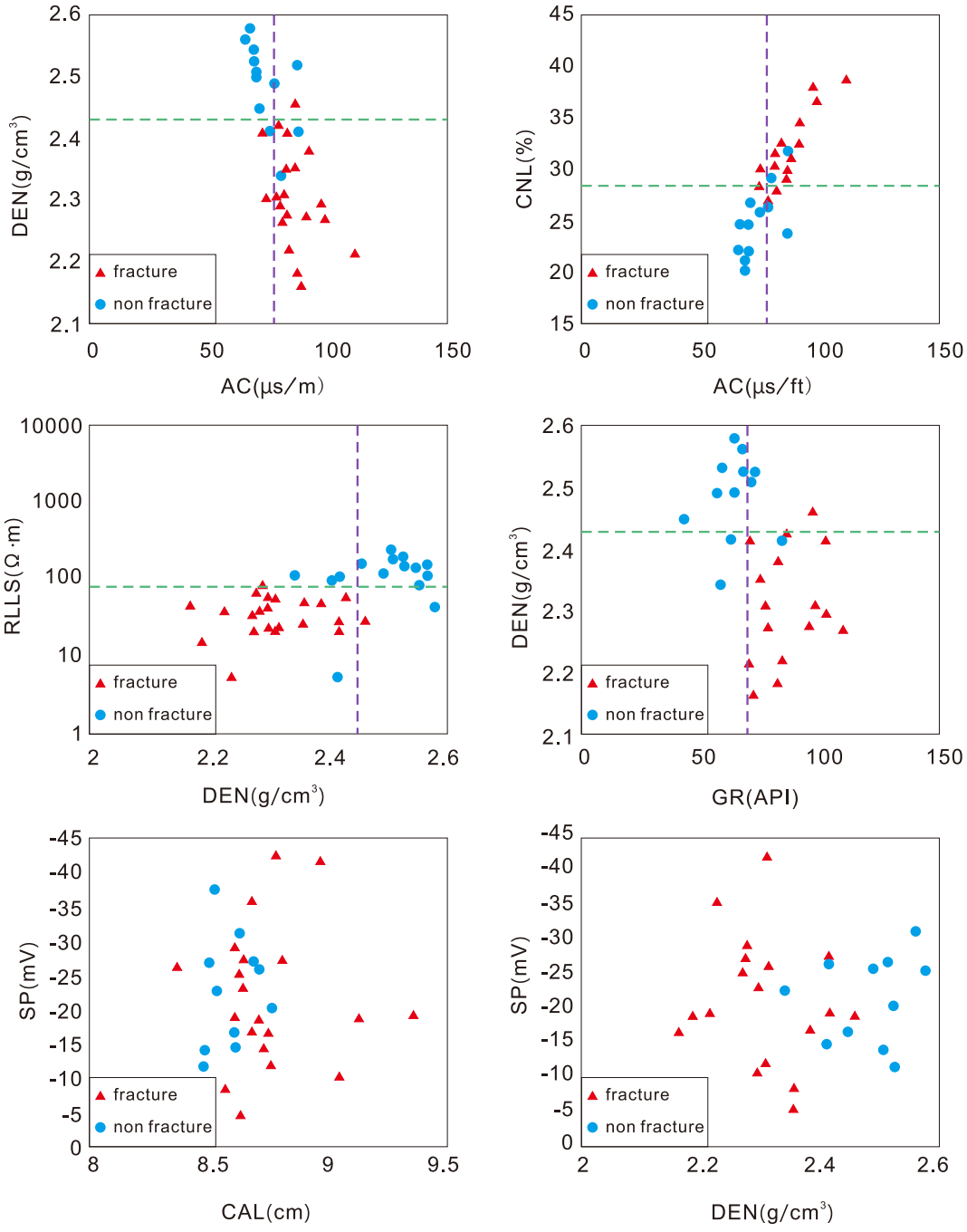

Fig. 6. The crossplot of conventional logging sequence.

Table 1
The main conventional logging sequence parameter statistics of 16 non-fracture sections.

Well no	Lithology	DEN (g·cm^{-3})	AC (μs/ft)	CNL (%)	RLLS (Ω·m)	GR (API)	CAL (cm)	SP (mv)
J22	limestone	2.576	66.2	24.73	42.94	63.9	8.716	−25.85
J22	mudstone	2.412	86.46	31.7	5.16	61.88	8.607	−14.87
J25	mudstone	2.545	67.85	21.13	134.5	51.76	8.523	−37.59
J27	mudstone	2.339	78.86	29.16	107.39	57.76	8.538	−22.83
J173	limestone	2.503	69.22	21.98	231	49.39	8.483	−14.23
J173	mudstone	2.524	68.18	20.26	143.6	67.8	8.479	−11.17
J36	mudstone	2.448	70.72	26.83	146.4	42.56	8.61	−16.87
J37	mudstone	2.413	74.86	26.05	101.9	82.9	8.5	−27.08
J37	mudstone	2.56	65.02	22.17	110.1	67.2	8.623	−31.44
J174	mudstone	2.49	76.88	26.59	114.44	63.61	8.7	−26.07
J174	mudstone	2.51	69.18	24.76	180.72	70.68	8.68	−27.01
J174	siltstone	2.52	85.98	23.92	172.34	72.3	8.76	−20.62
J30	siltstone	2.55			84.18		8.46	
J30	mudstone	2.56			140.69		8.732	
J31	marl	2.506			173.66		8.586	
J31	mudstone	2.403			94.24		8.621	

Table 2
The main conventional logging sequence parameter statistics of 23 fracture sections.

Well no	Lithology	DEN (g·cm^{-3})	AC (μs/ft)	CNL (%)	RLLS (Ω·m)	GR (API)	CAL (cm)	SP (mv)
J31	siltstone	2.285			82.19		8.883	
J31	siltstone	2.282			40.11		8.751	
J32	mudstone	2.293			58.39		9.22	
J34	siltstone	2.355	85.47	29.41	48.86	75.49	8.57	−5.41
J34	siltstone	2.353	81.51	28.14	26.82	75.54	8.44	−8.53
J36	marl	2.163	87.88	31.58	44.92	71.91	8.75	−16.97
J36	mudstone	2.185	86.61	31.38	15.53	81.49	9.12	−19.21
J36	sandstone	2.459	85.47	30.02	29.11	96.19	8.71	−19.15
J36	mudstone	2.413	82.04	30.46	28.23	69.91	8.61	−19.5
J37	siltstone	2.276	81.89	30.08	34.44	95.16	8.61	−29.54
J37	limestone	2.414	73.73	28.52	22.04	102.48	8.81	−27.9
J37	limestone	2.272	97.7	36.85	20.76	77.42	8.64	−27.76
J37	limestone	2.312	80.87	31.65	24.24	97.59	8.36	−26.82
J37	mudstone	2.268	80.34	30.39	35.26	109.34	8.62	−25.83
J37	siltstone	2.425	79.01	28.78	57.39	85.23	8.96	−42.22
J37	mudstone	2.307	77.84	27.37	54.71	76.19	8.78	−42.84
J29	mudstone	2.215	110.48	38.89	5.01	69.61	9.34	−19.81
J172	mudstone	2.222	83.17	32.71	37.89	83.45	8.67	−36.02
J174	siltstone	2.296	96.45	38.21	43.51	102.67	8.64	−23.39
J174	limestone	2.276	90.61	32.56	65.66	77.69	8.73	−14.97
J174	mudstone	2.295	78.86	29.51	23.14	101.94	9.04	−10.79
J174	limestone	2.307	73.52	30.53	20.55	97.57	8.76	−12.13
J174	limestone	2.382	91.21	34.63	48.31	81.89	8.68	−17.13

The white and black colors in the FMI images basically represent the high and low well wall resistivity respectively (Zeng et al., 2009; 2010, 2013; Lyu et al., 2016). The resistivity of drilling fluid is largely smaller than that of a stratigraphic section. Due to water-based drilling mud invasion, open fractures and closed fractures are generally seen as low (black) and high (white) resistivity respectively. For semi-filled fractures, the filled and open parts demonstrate high and low resistivity respectively. However, when there are no considerable differences between the properties of the fracture fill and the formation, the fractures are mainly identified by their appearance: they are randomly distributed and therefore show no obvious direction; they mostly appear with unclear margins and as highly variable dark patches in the image logs, whereas the bed interfaces are relatively continuous, have similar hydrodynamic characteristics, and generally have parallel high-conductivity anomalies. Image logging data were collected for almost all the wells within the Lucaogou Formation. In addition, image logging data can be used to quantitatively calculate the dip angle, porosity, and average width of the hydrodynamic effect of the fractures (Fig. 7). Regarding the fracture density, the concepts of absolute line density and relative line density are introduced to characterize the concentration of the fractures (Fig. 8). The calculation formula is as follows:

$$D_{alf} = \sum_{i=1}^{n} \left[\left(N_i \Big/ L_i \right) \right] / n \quad (1)$$

$$D_{rlf} = D_{alf} \left(\sum_{i=1}^{n} L_i \Big/ L_c \right) \quad (2)$$

where D_{alf} and D_{rlf} are the absolute line density and relative line density of the tectonic factures respectively, fractures/m; i represents a fractured interval; n is the total number of fractured intervals; N_i is the number of tectonic fractures in the ith fractured interval; L_i is the length of the ith fractured interval, m; and L_c is the total length of the core, m. The relative linear density of the tectonic fractures were counted (Fig. 9).

5. Results

5.1. Fluid inclusions

Fluid inclusions are the residual liquid from mineral crystallization. Measuring homogenization temperatures using fluid inclusions from fracture fillings is an effective method for investigating the timing of

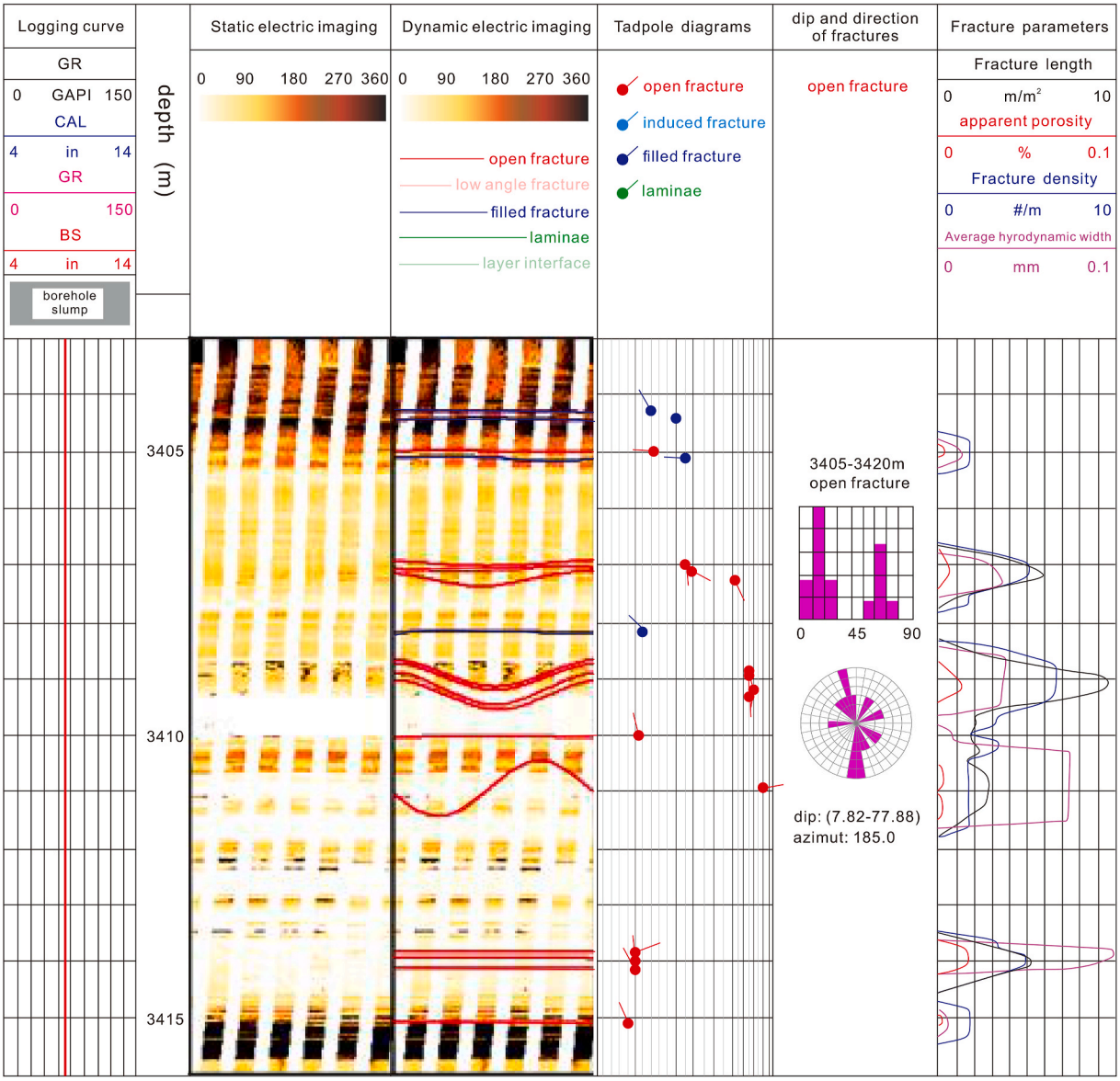

Fig. 7. Image logging data fracture parameter calculation from Well J25.

fracture formation (Laubach and Diaz-Tushman, 2009; Becker et al., 2010; Zeng et al., 2013; Zhang et al., 2020b). Therefore, we determined the homogenization temperatures of inclusions in the fillings of tectonic fractures that developed during different stages within the Lucaogou Formation tight reservoir (Fig. 10).

According to the measured homogenizing temperatures and salinity of inclusions from 110 secondary calcite samples (Table 3), three stages of hydrothermal activity can be determined (Fig. 11A and B). During Stage 1, the homogenization temperatures range from 31.7 to 45.0 °C, salinities range from 3.01 % to 4.95 %, and aqueous inclusions are dominant. During Stage 2, the homogeneity temperatures range between 50.1 and 64.6 °C with salinities between 8.49 % and 11.55 %, and the hydrocarbon inclusions are dominant. During Stage 3, the homogeneity temperatures range from 80.0 to 89.9 °C with salinities between 14.15 % and 22.96 %, and the hydrocarbon inclusions dominate. These measured samples were obtained from cores, and the homogeneity temperature and salinity results correspond to the three groups of fractures found in the cores. Therefore, based on the homogenization temperatures and salinities of the inclusion types, the tight reservoirs of the studied Formation have undergone at least three stages of fracturing and hydrothermal activity.

5.2. Ir element

Ir is a stable chemical trace element that has a very long half-life. Strata from different periods have differing Ir contents (Pearson and Woodland, 2000; Shinotsuka and Suzuki, 2007). Therefore, this element can be used to indicate the variations in the underground fluid environment. Calcite is the dominant fracture-filling mineral in the studied tight reservoirs in the Jimsar Sag, and the formation of the calcite is related to petroleum and other fluids. The natural fractures that formed during different stages are affected by late-stage fluid activity, and the earlier fracture fillings were formed during different times; therefore, the fillings contain different Ir values. Testing and analysis of the Ir content of the calcite fracture fillings from 87 sampling points show that the Ir contents generally range between 11.67×10^{-12} and 28.93×10^{-12} g/g (Table 4), and can be divided into three intervals (Fig. 12). Interval I contains 28 samples that generally have Ir contents between 11.67×10^{-12} and 15.91×10^{-12} g/g, accounting for 32.18 % of the samples; Interval II contains 25 samples that generally have Ir contents between 18.73×10^{-12} and 22.94×10^{-12} g/g, accounting for 28.74 % of the samples; and Interval III contains 34 samples that generally have Ir contents between 25.09×10^{-12} and 28.93×10^{-12} g/g, accounting

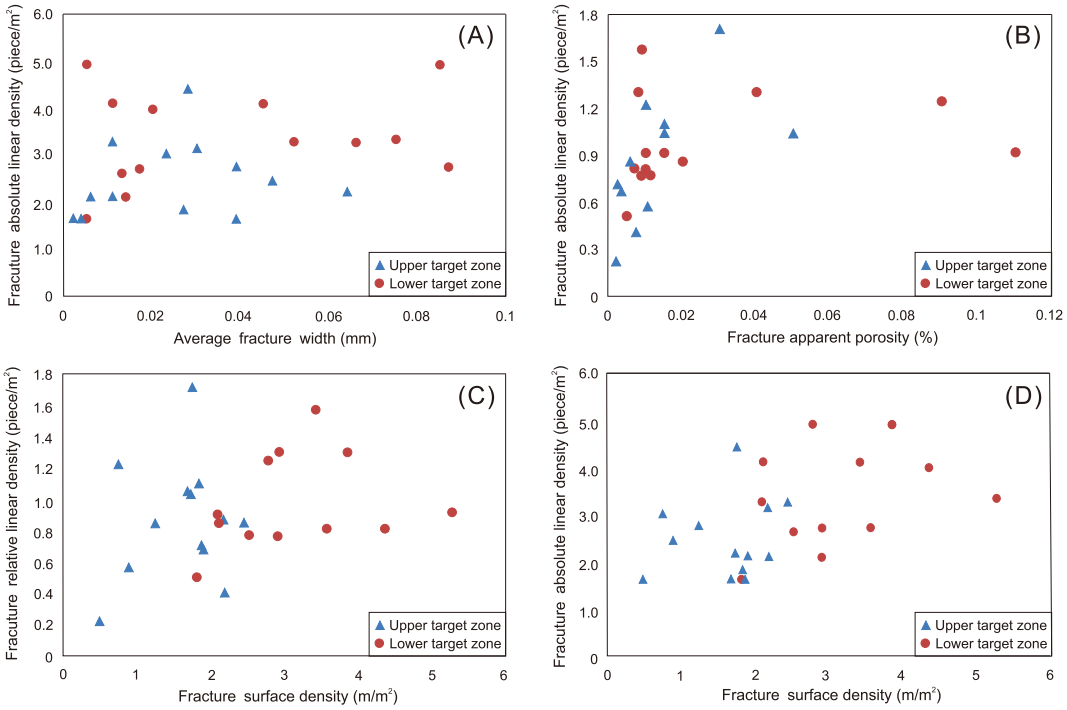

Fig. 8. (A) Crossplot of the average width and the absolute line density of the fractures; (B) Crossplot of the interstitial density and the absolute line density of the fractures; (C) Crossplot of the density and the relative line density of the fractures; (D) Crossplot of the density and the absolute line density of the fractures.

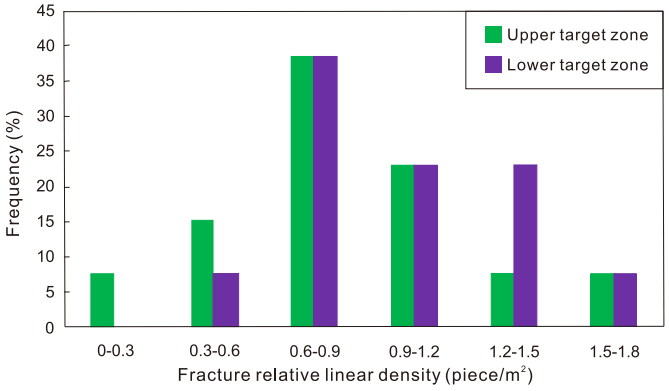

Fig. 9. Histogram of the distribution of the relative linear density of the tectonic fractures.

for 39.08 % of the samples. These distributions of Ir (geochemical trace element) indicate that the fractures in the studied tight reservoirs formed during three stages. However, Ir can only be used to determine the number of stages of fracture development and cannot be used to determine the formation sequence of the fractures. Therefore, the results need to be combined with those of isotopic analyses to further confirm the specific time of formation of these fractures.

5.3. C and O stable isotopes

C and O stable isotopes of calcite are principally affected by the temperature and salinity of the associated media. During diagenesis, the burial depth, temperature, pressure, and organic matter (OM) decomposition of sediments have particular impacts on the $\delta^{13}C$ and $\delta^{18}O$ values. Fracture systems alter after each successive tectonic activity, and during such changes, formation water charges, mineral crystals precipitate onto the fracture walls, and multistage cements adhere to the fracture walls during multiphase mineralized water flows (Naehr et al., 2007; Gieskes et al., 2005; Loyd et al., 2016). Fluid inclusions formed during different periods contain different mineral compositions, and the $\delta^{13}C$ and $\delta^{18}O$ values of different stages of fracture filling vary. The $\delta^{13}C$ and $\delta^{18}O$ values of the fracture-filling calcite can be analyzed, and the different filling stages of the fractures can be determined. Ultimately, the stages of fracturing can be inferred.

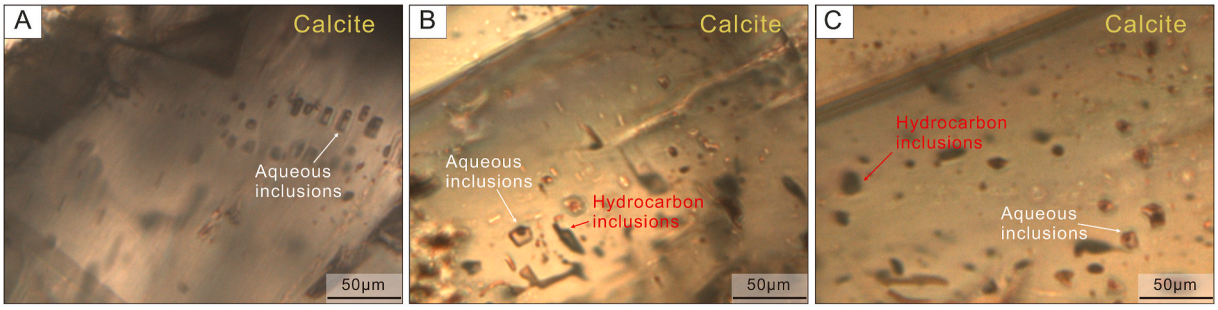

Fig. 10. Microphotographs under plane-polarized light of representative fluid inclusions in calcite veins in the Lucaogou Formation: (A) aqueous inclusions in calcite veins; (B) hydrocarbon inclusions coexisting with little aqueous inclusions in calcite veins; (C) hydrocarbon inclusions coexisting with little aqueous inclusions in calcite veins.

Table 3
Fluid inclusion homogenization and salinity composition of calcite fracture fills.

Sample	Testing position	Cause	Types	Size	Gas-liquid ratio	Temperature	Salinity
	Calcite vein	Secondary	gas–liquid inorganic salt water inclusions	8.8	< 5	34.8	3.44
	Calcite vein	secondary	gas–liquid inorganic salt water inclusions	10.1	< 5	34.4	3.4
	Calcite vein	secondary	gas–liquid organic inclusions	4.9	< 5	38.8	3.86
	Calcite vein	secondary	gas–liquid inorganic salt water inclusions	7.1	< 5	38.5	3.76
	Calcite vein	secondary	gas–liquid organic inclusions	7.2	< 5	36.2	3.72
	Calcite vein	secondary	gas–liquid inorganic salt water inclusions	7.6	< 5	39.6	4
	Calcite vein	secondary	gas–liquid inorganic salt water inclusions	5.5	< 5	18.3	1.59
	Calcite vein	secondary	gas–liquid inorganic salt water inclusions	4.1	< 5	32.9	3.19
	Calcite vein	secondary	gas–liquid inorganic salt water inclusions	3.9	< 5	43.3	3.31
	Calcite vein	secondary	gas–liquid inorganic salt water inclusions	4.1	< 5	41.3	4.24
	Calcite vein	secondary	gas–liquid organic inclusions	7.1	< 5	52.2	8.95
	Calcite vein	secondary	gas–liquid organic inclusions	9.9	< 5	51.8	8.63
	Calcite vein	secondary	gas–liquid organic inclusions	4.9	< 5	54.1	9.2
	Calcite vein	secondary	gas–liquid organic inclusions	8.2	< 5	54.2	9.5
	Calcite vein	secondary	gas–liquid organic inclusions	6.3	< 5	44.1	4.8
	Calcite vein	secondary	gas–liquid organic inclusions	8.2	< 5	44.6	3.82
	Calcite vein	secondary	gas–liquid organic inclusions	10.2	< 5	57.1	10.19
	Calcite vein	secondary	gas–liquid inorganic salt water inclusions	9.9	< 5	57.1	10.06
	Calcite vein	secondary	gas–liquid organic inclusions	10.4	< 5	54.5	9.67
	Calcite vein	secondary	gas–liquid inorganic salt water inclusions	8	< 5	55	9.71
	Calcite vein	secondary	gas–liquid organic inclusions	8	< 5	56.9	9.93
	Calcite vein	secondary	gas–liquid organic inclusions	6.5	< 5	45	4.95
	Calcite vein	secondary	gas–liquid organic inclusions	8.4	< 5	48.3	6.69
	Calcite vein	secondary	gas–liquid inorganic salt water inclusions	3.1	< 5	40.8	4.05
	Calcite vein	secondary	gas–liquid organic inclusions	5.3	< 5	39.6	4.87
	Calcite vein	secondary	gas–liquid inorganic salt water inclusions	6.9	< 5	35	4.54
	Calcite vein	secondary	gas–liquid inorganic salt water inclusions	3.6	< 5	35.2	3.58
	Calcite vein	secondary	gas–liquid inorganic salt water inclusions	4.7	< 5	21.2	2.69
	Calcite vein	secondary	gas–liquid inorganic salt water inclusions	5.8	< 5	31.7	3.01
	Calcite vein	secondary	gas–liquid inorganic salt water inclusions	3.1	< 5	33.1	4.24
	Calcite vein	secondary	gas–liquid inorganic salt water inclusions	8.8	< 5	35.7	4.13
	Calcite vein	secondary	gas–liquid inorganic salt water inclusions	7.9	< 5	34.2	3.28
	Calcite vein	secondary	gas–liquid inorganic salt water inclusions	9.8	< 5	43.6	4.47
	Calcite vein	secondary	gas–liquid organic inclusions	8.7	< 5	43.7	3.75
	Calcite vein	secondary	gas–liquid inorganic salt water inclusions	8.7	< 5	43.7	3.75
	Calcite vein	secondary	gas–liquid inorganic salt water inclusions	6.3	< 5	38.3	3.13
	Calcite vein	secondary	gas–liquid inorganic salt water inclusions	15.6	< 5	38.6	3.85
	Calcite vein	secondary	gas–liquid organic inclusions	6.5	< 5	52.8	9.08
	Calcite vein	secondary	gas–liquid organic inclusions	3.1	< 5	53	9.1
	Calcite vein	secondary	gas–liquid inorganic salt water inclusions	8.4	< 5	53.9	10.71
	Calcite vein	secondary	gas–liquid organic inclusions	9.4	< 5	50.1	9.21
	Calcite vein	secondary	gas–liquid organic inclusions	11.8	< 5	50.5	10.1
	Calcite vein	secondary	gas–liquid organic inclusions	5.3	< 5	50.8	8.52
	Calcite vein	secondary	gas–liquid inorganic salt water inclusions	7.5	< 5	52.3	9.01
	Calcite vein	secondary	gas–liquid organic inclusions	5.3	< 5	73.7	18.19
	Calcite vein	secondary	gas–liquid organic inclusions	9	< 5	77.2	12.21
	Calcite vein	secondary	gas–liquid organic inclusions	5.6	< 5	63.7	9.67
	Calcite vein	secondary	gas–liquid inorganic salt water inclusions	8.4	< 5	80	17.17
	Calcite vein	secondary	gas–liquid organic inclusions	8.6	< 5	80.3	22.96
	Calcite vein	secondary	gas–liquid inorganic salt water inclusions	6.7	< 5	80.8	15.21
	Calcite vein	secondary	gas–liquid inorganic salt water inclusions	4.7	< 5	80.8	19.47
	Calcite vein	secondary	gas–liquid organic inclusions	4.8	< 5	59.6	11.25
	Calcite vein	secondary	gas–liquid organic inclusions	5.6	< 5	60.2	11.31
	Calcite vein	secondary	gas–liquid organic inclusions	5	< 5	60.8	10.8
	Calcite vein	secondary	gas–liquid organic inclusions	7.8	< 5	58.9	10.31
	Calcite vein	secondary	gas–liquid inorganic salt water inclusions	9.2	< 5	61.2	8.82
	Calcite vein	secondary	gas–liquid organic inclusions	4.8	< 5	61.5	11.55
	Calcite vein	secondary	gas–liquid organic inclusions	8	< 5	61.9	8.55
	Calcite vein	secondary	gas–liquid organic inclusions	4.8	< 5	57.3	10.25
	Calcite vein	secondary	gas–liquid inorganic salt water inclusions	4	< 5	58.1	9.41
	Calcite vein	secondary	gas–liquid inorganic salt water inclusions	9.6	< 5	58.8	9.6
	Calcite vein	secondary	gas–liquid inorganic salt water inclusions	8.1	< 5	83.3	20.73
	Calcite vein	secondary	gas–liquid inorganic salt water inclusions	9.8	< 5	83.4	16.24
	Calcite vein	secondary	gas–liquid inorganic salt water inclusions	5.3	< 5	83.7	20.03
	Calcite vein	secondary	gas–liquid organic inclusions	11.2	< 5	85.5	21.28
	Calcite vein	secondary	gas–liquid organic inclusions	10.3	< 5	85.7	14.31
	Calcite vein	secondary	gas–liquid organic inclusions	6.6	< 5	85.7	17.07
	Calcite vein	secondary	gas–liquid organic inclusions	7	< 5	85.1	20.33
	Calcite vein	secondary	gas–liquid organic inclusions	9.7	< 5	84.7	16.79
	Calcite vein	secondary	gas–liquid organic inclusions	4.2	< 5	67.3	13.42
	Calcite vein	secondary	gas–liquid inorganic salt water inclusions	6	< 5	79.4	14.51
	Calcite vein	secondary	gas–liquid organic inclusions	11.4	< 5	88.3	20.27
	Calcite vein	secondary	gas–liquid organic inclusions	7.1	< 5	88.1	16.42
	Calcite vein	secondary	gas–liquid inorganic salt water inclusions	12.3	< 5	88.6	16.14

(*continued on next page*)

Table 3 (*continued*)

Sample	Testing position	Cause	Types	Size	Gas-liquid ratio	Temperature	Salinity
	Calcite vein	secondary	gas–liquid organic inclusions	7.5	< 5	84.1	22.42
	Calcite vein	secondary	gas–liquid organic inclusions	9.1	< 5	84.2	14.15
	Calcite vein	secondary	gas–liquid organic inclusions	9.9	< 5	83.7	15.86
	Calcite vein	secondary	gas–liquid organic inclusions	7.3	< 5	84.6	16.85
	Calcite vein	secondary	gas–liquid organic inclusions	4.9	< 5	84.9	19.14
	Calcite vein	secondary	gas–liquid organic inclusions	9	< 5	83.8	21.14
	Calcite vein	secondary	gas–liquid organic inclusions	7.2	< 5	81.3	15.06
	Calcite vein	secondary	gas–liquid organic inclusions	6.6	< 5	81.7	20.55
	Calcite vein	secondary	gas–liquid organic inclusions	8.5	< 5	82.3	21.68
	Calcite vein	secondary	gas–liquid organic inclusions	8.4	< 5	83	15.6
	Calcite vein	secondary	gas–liquid organic inclusions	5	< 5	80.8	21.98
	Calcite vein	secondary	gas–liquid organic inclusions	5	< 5	81.3	16.21
	Calcite vein	secondary	gas–liquid organic inclusions	7	< 5	62	9.87
	Calcite vein	secondary	gas–liquid inorganic salt water inclusions	5.1	< 5	63.5	8.87
	Calcite vein	secondary	gas–liquid organic inclusions	9.5	< 5	67.3	12.99
	Calcite vein	secondary	gas–liquid organic inclusions	11.4	< 5	57.3	10.34
	Calcite vein	secondary	gas–liquid inorganic salt water inclusions	9.3	< 5	58.8	9.76
	Calcite vein	secondary	gas–liquid organic inclusions	8.7	< 5	59.1	8.41
	Calcite vein	secondary	gas–liquid organic inclusions	8.1	< 5	59.4	11.19
	Calcite vein	secondary	gas–liquid organic inclusions	7.4	< 5	64.6	11.87
	Calcite vein	secondary	gas–liquid inorganic salt water inclusions	6.8	< 5	85.8	21.93
	Calcite vein	secondary	gas–liquid organic inclusions	8.3	< 5	86.9	15.19
	Calcite vein	secondary	gas–liquid organic inclusions	5.3	< 5	85.1	16.59
	Calcite vein	secondary	gas–liquid organic inclusions	10.7	< 5	85.4	16.51
	Calcite vein	secondary	gas–liquid organic inclusions	6.6	< 5	87.2	14.69
	Calcite vein	secondary	gas–liquid organic inclusions	7.6	< 5	86.1	22.52
	Calcite vein	secondary	gas–liquid organic inclusions	8.1	< 5	86.3	18.31
	Calcite vein	secondary	gas–liquid organic inclusions	12.6	< 5	91	24.57
	Calcite vein	secondary	gas–liquid organic inclusions	9.3	< 5	89.9	21.37
	Calcite vein	secondary	gas–liquid organic inclusions	8.3	< 5	89.2	19.77
	Calcite vein	secondary	gas–liquid inorganic salt water inclusions	9.2	< 5	92.9	25.31
	Calcite vein	secondary	gas–liquid organic inclusions	8.8	< 5	97.9	25.78
	Calcite vein	secondary	gas–liquid organic inclusions	12.1	< 5	97.3	27.88
	Calcite vein	secondary	gas–liquid organic inclusions	10.6	< 5	97.5	19.12
	Calcite vein	secondary	gas–liquid organic inclusions	8.2	< 5	93.8	21.98
	Calcite vein	secondary	gas–liquid organic inclusions	7.9	< 5	89.1	22.31

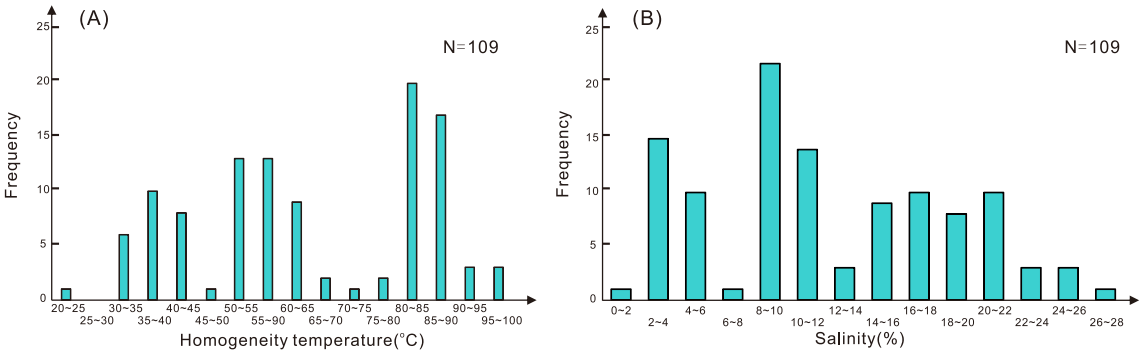

Fig. 11. (A) Homogeneity temperature and frequency of calcite-filled fractures in the Lucaogou Formation; (B) Salinity and frequency of calcite-filled fractures in the Lucaogou Formation.

Therefore, to infer the formation stages of the fractures, 16 pieces of core fracture-filling samples from 16 wells were selected for C and O stable isotope testing and analysis (Table 5). The C–O isotope distribution diagram shows that the samples can be divided into three intervals, with respective average values of corresponding O isotopes of −7.99 ‰, −9.97 ‰, and −12.42 ‰ (Fig. 13), representing the formation of fractures during three stages. The formation temperatures of the fractures were calculated using the temperature measurement equation for the O isotope proposed by Epstein and Mayeda(1953) as follows:

$$t = 31.9 - 5.55\left(\delta^{18}O - \delta^{18}O_w\right) + 0.7\left(\delta^{18}O - \delta^{18}O_w\right)^2 \quad (2)$$

where t is the formation temperature of the calcite, $\delta^{18}O$ is the O isotopic value of the mineral (‰), and $\delta^{18}O_w$ is the O isotopic value of the water when the mineral is formed (‰). By also considering the surface temperature and geothermal gradient, the paleo-burial depth of fracture formation can then be estimated. Finally, combining these results with the stratigraphic burial depth evolution of the basin, specific formation times of the various fracture stages can then be determined.

The Permian Lucaogou Formation is present in a saline lake basin environment, and the average water isotope value is generally assumed to be −7‰. Using this value and the measured values of the various stages of O isotopes, the formation temperatures of the three stages of fracturing can be calculated as 38.1 °C, 54.6 °C, and 82.6 °C.

5.4. Acoustic emissions

The count of Kaiser impact points along the AE curve of an AE experiment can then be used to determine i) the stages when minimum stress occurred and ii) the associated stress field experienced by the rock

Table 4
Ir composition of calcite fracture fills.

Sample	Testing position	Ir element content
	Calcite vein	27.42
	Calcite vein	27.93
	Calcite vein	27.83
	Calcite vein	27.78
	Calcite vein	27.21
	Calcite vein	27.86
	Calcite vein	27.81
	Calcite vein	19.35
	Calcite vein	27.23
	Calcite vein	27.87
	Calcite vein	28.55
	Calcite vein	28.93
	Calcite vein	28.42
	Calcite vein	28.25
	Calcite vein	28.2
	Calcite vein	27.86
	Calcite vein	28
	Calcite vein	27.6
	Calcite vein	27.86
	Calcite vein	27.81
	Calcite vein	27.04
	Calcite vein	27.23
	Calcite vein	27.69
	Calcite vein	26.1
	Calcite vein	26.29
	Calcite vein	26.72
	Calcite vein	26.98
	Calcite vein	26.45
	Calcite vein	26.37
	Calcite vein	25.2
	Calcite vein	25.09
	Calcite vein	25.91
	Calcite vein	25.85
	Calcite vein	25.78
	Calcite vein	25.33
	Calcite vein	15.56
	Calcite vein	14.65
	Calcite vein	14.98
	Calcite vein	14.51
	Calcite vein	14.59
	Calcite vein	14.82
	Calcite vein	14.4
	Calcite vein	14.67
	Calcite vein	14.7
	Calcite vein	14.4
	Calcite vein	15.65
	Calcite vein	14.65
	Calcite vein	15.3
	Calcite vein	14.14
	Calcite vein	13.88
	Calcite vein	13.93
	Calcite vein	12.29
	Calcite vein	12.8
	Calcite vein	15.03
	Calcite vein	12.27
	Calcite vein	11.67
	Calcite vein	13.95
	Calcite vein	21.67
	Calcite vein	22.79
	Calcite vein	20.22
	Calcite vein	20.31
	Calcite vein	21
	Calcite vein	19.98
	Calcite vein	22.47
	Calcite vein	22.06
	Calcite vein	21.08
	Calcite vein	19.66
	Calcite vein	18.73
	Calcite vein	20.06
	Calcite vein	21.25
	Calcite vein	19.82
	Calcite vein	19.03
	Calcite vein	19.04
	Calcite vein	20.59
	Calcite vein	20.08
	Calcite vein	20.47
	Calcite vein	20.46
	Calcite vein	20.68
	Calcite vein	20.91
	Calcite vein	22.94
	Calcite vein	22.72
	Calcite vein	12.58
	Calcite vein	13.33
	Calcite vein	15.6
	Calcite vein	14.88
	Calcite vein	15.91
	Calcite vein	12.06

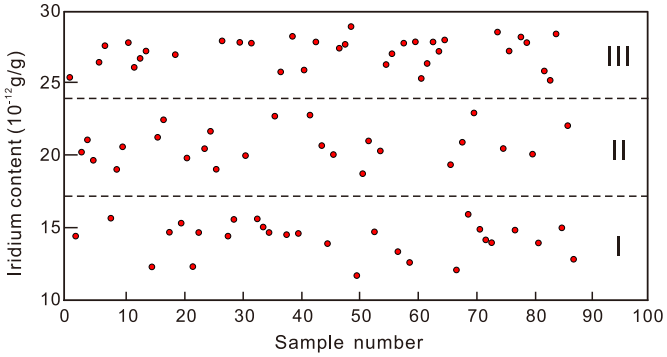

Fig. 12. Sample number and Iridium content of calcite-filled fractures in the Lucaogou Formation.

formation. However, the locations of these points on the AE curve correspond to step-like, sharply increasing locations, but the earlier and later steps do not represent the sequence of these points. Fig. 14 (except Fig. 14K) shows that the core samples generally have four Kaiser effect points, implying that the strata from which the samples were collected underwent at least four stages of fracturing. These four points generally have a certain range of variation in the stress field, indicating that the fractures (microfractures) related to the four points resulted from tectonism. However, only three types of fractures were recognized in the cores, possibly showing that two stages of tectonism produced two groups of fractures with the same attitudes. The results show that the study area underwent four stages of tectonism, which produced four stages of fracture filling, with two stages having the same or similar orientation.

5.5. Conventional logging and image logging

A cross analysis was conducted, mainly employing the main conventional logging suites for the fractured and non-fractured intervals (Fig. 6). The fractured intervals in the study area predominantly show the following conventional response characteristics: the GR counting rate increases slightly; the SP and CAL curves show no clear responses to fractures; the resistivity values are lower in the fractured intervals than in the non-fractured intervals, and the deep neutron resistivity difference value is relatively low; the formation density clearly decreases; the acoustic travel time greatly increases; the “cycle-skip” characteristics are not apparent; and the neutron porosity clearly increases.

The conventional logging suite shows a strong response to fractures in the study area. The main logging techniques used included DEN, AC, CNL, natural GR, and shallow lateral resistivity logging. These techniques were used because thin interbeds spread extensively in the study area, and the impact of lithology on the SP and borehole diameter exceed that of the fractures; furthermore, the fracture dip angles vary greatly, and the deep and shallow lateral resistivity value difference is

Table 5
Carbon and oxygen isotopic composition of calcite fracture fills.

Sample	Well no.	Buried depth/m	Core lithology	Testing position	$\delta^{13}C$ (PDB)	$\delta^{18}O$ (PDB)	Salinity index	Formation temperature (°C)
JM-3	J30	3929.2	Muddy limestone	Calcite vein	3.42	−10.103	130.288	55.862
JM-6	J30	4082.6	Silt	Calcite vein	2.036	−9.856	133.395	53.461
JM-14	J30	4051.1	Silt	Calcite vein	−0.513	−7.339	127.451	33.862
JM-32	J32	3900.1	Muddy limestone	Calcite vein	2.997	−10.749	136.527	62.545
JM-45	J32	3781.1	Finestone	Calcite vein	6.149	−12.471	134.093	83.216
JM-49	J32	3766.8	Dolomite	Calcite vein	0.159	−7.845	123.550	37.090
JM-57	J174	3632.5	Limestone	Calcite vein	5.812	−12.187	136.437	79.521
JM-69	J174	3608.2	Silt	Calcite vein	2.965	−9.538	135.633	50.495
JM-70	J174	3571.3	Dolomite	Calcite vein	−0.316	−8.317	131.824	40.423
JM-86	J251	3356.8	Silt	Calcite vein	3.578	−9.772	130.789	52.663
JM-92	J251	3111.0	Muddy limestone	Calcite vein	7.03	−12.683	123.499	86.048
JM-104	J251	2901.6	Finestone	Calcite vein	−0.476	−8.632	129.259	42.822
JM-107	J251	2744.9	Silt	Calcite vein	0.214	−7.012	124.563	31.967
JM-111	J15	2741.7	Limestone	Calcite vein	2.741	−9.801	134.122	52.937
JM-123	J15	2662.6	Silt	Calcite vein	0.997	−8.812	121.855	44.255
JM-129	J15	2484.0	Muddy limestone	Calcite vein	6.578	−12.355	126.769	81.693

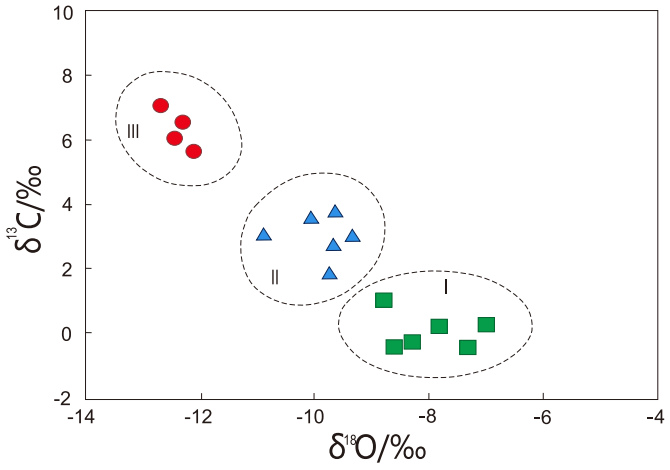

Fig. 13. Carbon and oxygen isotope values of calcite-filled fractures in the Lucaogou Formation.

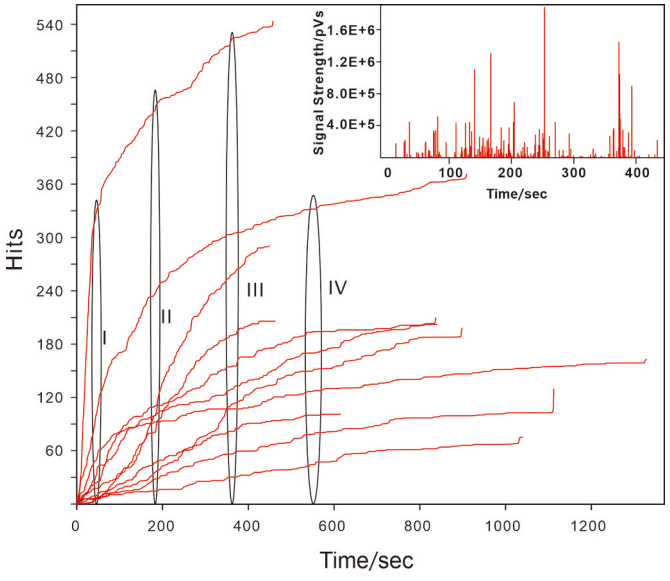

Fig. 14. Acoustic emission curve from non-directional reservoir rocks.

relatively small. Therefore, it is not possible to distinguish the fractured intervals in the study area.

Image logging interpretation results show that the fractures in the study area are dominated primarily by bedding-parallel fractures. There are weak variations between the absolute line densities, and apparent porosities of the fractures of target zones (Fig. 8A and B): the absolute line densities of fractures vary within 1–5 fractures/m, the widths are <0.1 mm, and the apparent porosity is generally <0.04 %. Compared to the upper target zone, there is an increase in the fracture area density in the lower target zone (Fig. 8C and D): the fracture area density in the lower target zone is up to 2–5 fractures/m, which is related to the greater concentration of fractures in sub-layers. Furthermore, there is a slight difference in the relative line density of fractures in the lower target zone compared to the upper target zone: the relative line density in the lower target zone generally tends to be greater, and the percentage of >1 fracture/m is above 50 % (Fig. 9).

6. Discussion

6.1. Sequence of formation of fractures with variable mechanical origins

Observing the crosscutting, abutting, and coalescence relations among the core fractures is the most direct and effective method of analyzing the fracture stages. From the observations of the cores from 22 wells in the Jimsar Sag, fractures from the target horizon in the study area are filled with varying degrees, and the fillings are dominantly calcite with minor argillaceous matter and pyrite. Our results indicate that there are principally three groups of tectonic fractures in the target zone of the Lucaogou Formation: the first group comprises short moderate–high-angle fractures (with dip angles of 50°–70°) that are mostly extension fractures with widths of 0.5–2 mm; this group of fractures is nearly completely filled, mainly with calcite with minor argillaceous matter (Fig. 3C). The second group comprises inclined and subvertical fractures (with dip angles mostly above 70°), which are longer than can be measured in the core, with planar fracture walls. Shear fractures dominate, and fracture apertures are generally <1 mm. In this group of fractures, one or several of the fractures generally cut through the bedding-parallel fractures, or fractures that have consistently similar attitudes occur in a group (Fig. 3D); these fractures are predominantly fully filled or partially-filled; many types of fillings are observed, but calcite dominates, while some sections are filled with pyrite. The third group comprises bedding-parallel oblique crossing fractures (15–30°), which are very long and predominantly shear fractures (Fig. 3A and B). The fracture apertures are relatively large (generally >1 mm). In these fractures, the filling degree is relatively low, with calcite and argillaceous matter occasionally observable, and most of the fractures contain oil and gas shows. This is the better developed group of fractures in the

study area.

In addition to the considerable differences in fracture attitudes and filling properties, these different groups of fractures also have very different crosscutting and abutting relations. In the cores, the bedding-parallel shear fractures usually about the inclined shear fractures and inclined extension fractures. For example, in the 3594.60–3594.73 m core section from Well J251 (Fig. 3A), one bedding-parallel shear fracture filled with calcite is crosscut by an inclined extension fracture. In the core section of 3223.31–3223.56 m in Well J174 (Fig. 3B), one bedding-parallel shear fracture is crosscut by an inclined shear fracture. The inclined extension fractures and shear fractures are basically calcite-filled and more sparsely filled respectively.

It can thus be preliminarily determined that inclined extension and shear fractures are early-stage fractures and that bedding-parallel shear fractures are late-stage fractures.

6.2. *Matching the development stages of tectonic fractures with the tectonic evolution history*

Calibration of chemical properties of fracture fillings is of considerable significance in the determination of fracture formation stages and their paleo-physical and chemical environments. When rocks break due to tectonic stress, formation water enters the fractures, and crystalline minerals precipitate out of the fluid and between the fracture walls. Therefore, the geochemical and isotopic characteristics of fracture fillings can be used to effectively analyze the stages of fracturing.

Information pertaining to the dip angle of the fractures in the upper and lower target zone intervals was obtained from the image logging data of ten wells (such as J36 and J37). The results show that the fractures in the lower and upper target zone intervals are basically consistent in strike, with variable dips (Fig. 14B). This indirectly indicates that fractures within different horizons were produced spatially in a consistent tectonic setting within the study area, and that the fractures within the upper and lower target zone intervals developed with similar orientations during corresponding stages. According to the strike data of the tectonic fractures in various wells, a plan view rose diagram of the strikes of the tectonic fractures and a general rose diagram of the strikes of the tectonic fractures were compiled. The tectonic fracture strike rose diagram shows that, in the study area, three evident fracture groups are present with different striking directions: ENE-striking, NNW-striking, and nearly N–S-striking fractures (Fig. 15A and C). In plan view, the three groups of fractures show certain regularities: the ENE-striking fractures are distributed in the middle and south of the sag; the nearly N–S-striking fractures mainly occur in the north and east; and the NNW-striking fractures are widely and relatively less distributed. According to the shapes and crosscutting relationships of the fractures determined by the field observations, the fractures formed in the following order: the nearly N–S-striking extension fractures (striking 0°–27°), the ENE-striking shear fractures (45°–63°), and finally the NNW-striking shear fractures (317°–345°).

In general, in the fracture fillings, all the $\delta^{18}O$ values are negative and all the $\delta^{13}C$ values are positive, but these values have large ranges ($\delta^{13}C$ ranges from −0.513 to 7.030 ‰ and $\delta^{18}O$ ranges from −12.683 to −7.012 ‰). The $\delta^{13}C$ values increase with respect to the changes in the strength of the tectonic stages or diagenesis (Table 5), and the $\delta^{18}O$ values show a negative trend and display inherited evolutionary characteristics. To determine when the fracture fillings crystallized and formed, the $\delta^{18}O$ values were selected as reference values when conducting the temperature measurements and calculations.

The calcite fillings in the Stage 1 fractures have $\delta^{18}O$ values ranging from −7.012 ‰ to −8.812 ‰, and $\delta^{13}C$ values ranging from −0.513 ‰ to 0.997 ‰. Temperature calculation using the $\delta^{18}O$ values provides results between 31.967 and 44.255 °C. The average burial depth during fracture filling was 863 m (Fig. 16); therefore, this stage of fracturing occurred during the late Triassic, and is the product of the Indosinian Movement. The Junggar Basin experienced intense tectonism in the late Triassic and transformed from a faulted setting to a compressional setting (Wang et al., 2016a,b; Liu et al., 2017, 2018, 2018; Zhu et al., 2017; Zhang et al., 2020c). The exhumation of the sediments led to a decrease in confining pressure, generating numerous N–S-striking extension fractures.

The calcite fillings of the Stage 2 fractures have $\delta^{18}O$ values ranging from −9.538 ‰ to −10.749 ‰, and $\delta^{13}C$ values ranging from 2.036 ‰ to 3.578 ‰. According to our calculations, the formation temperatures range from 50.495 to 62.545 °C, and the burial depths during fracture filling averaged 2095 m (Fig. 16); therefore, this stage of fracturing occurred during the Middle−Late Jurassic, and the fillings are products of Episode II of the Yanshanian Movement. During this time, the Tianshan area underwent intense tectonism and fast uplifting. The basin margins moved northward, and an evolutionary stage dominated by compressional regime began (Hu et al., 2016a; Dong et al., 2015). The western segment of the Fukang fault belt produced SW−NE compressive stress, forming ENE-striking shear fractures.

The calcite fillings of the Stage 3 fractures have $\delta^{18}O$ values ranging

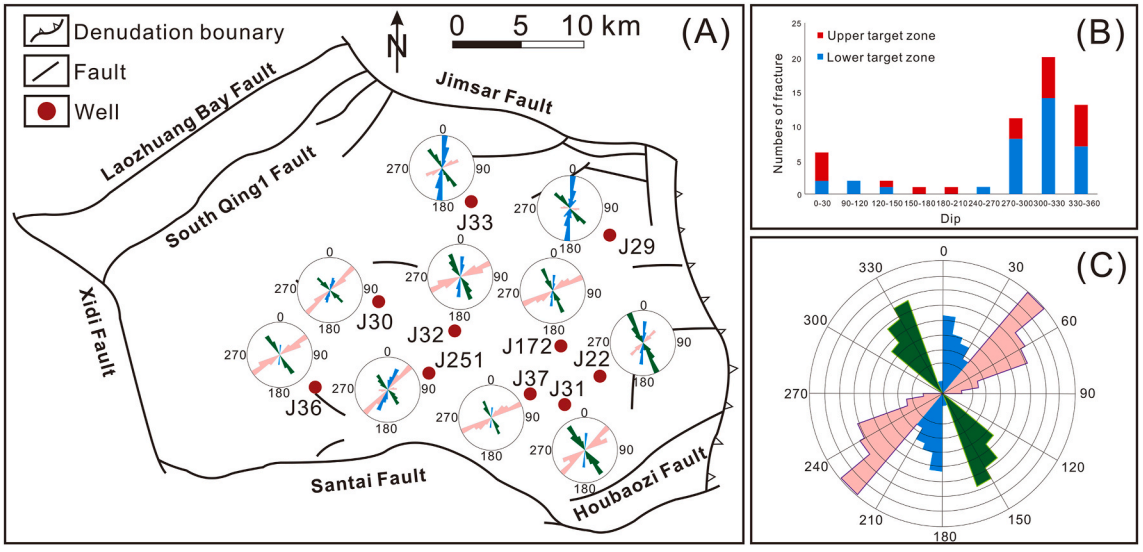

Fig. 15. Rose diagram showing strike of joints based on well log image; (A) rose diagram of 10 wells (J33, J29, J30, J36, J32, J251, J172, J37, J22, and J31); (B) Histogram of tectonic fractures in different dips in J36; (C) rose diagram showing joints in all 10 wells.

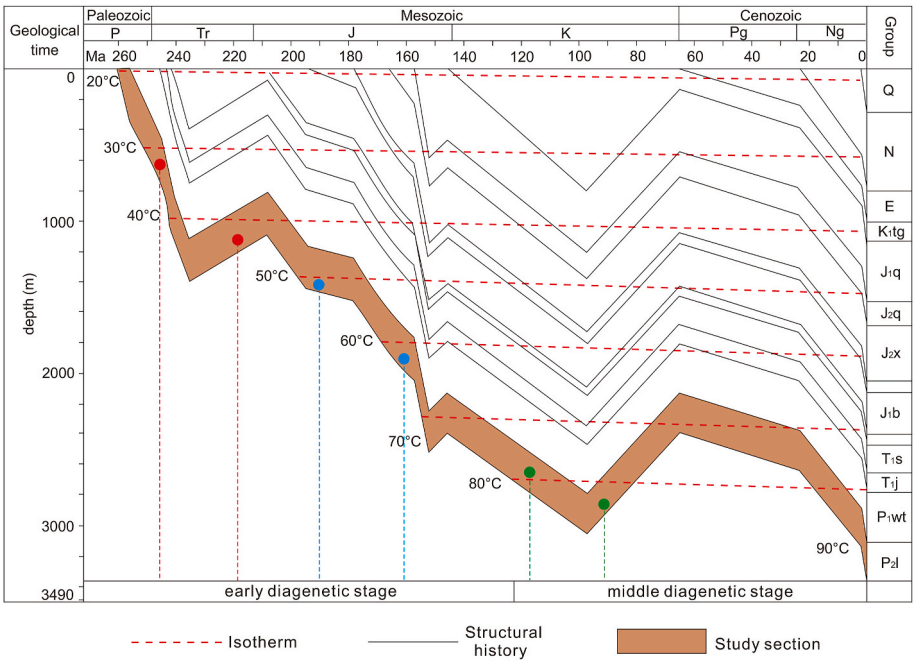

Fig. 16. Burial history of the tight Lucaogou oil reservoirs (modified after Wu et al., 2016).

from −12.187 ‰ to −12.683 ‰, and $\delta^{13}C$ values ranging from 5.812 ‰ to 7.130 ‰. The formation temperatures of the fillings range from 79.521 to 86.048 °C, and the burial depth during the formation of the fracture fillings averaged at 2845 m (Fig. 16); therefore, this stage of fracturing occurred during the Cretaceous, and the fillings are products of Episode III of the Yanshanian Movement. During the Early Cretaceous, the Bogda piedmont foreland sag experienced continuous folding under the tectonic stress (Sui, 2015; Huang et al., 2018), the southern Fukang fault belt was very active (Ji et al., 2017), and intense compressive nappe characteristics were expressed from north to south, forming NNW-striking shear fractures. In the Himalayan period, the Tianshan Mountains reserved the tectonic system of Episode III of the Yanshanian Movement (Ma et al., 2015; Yi et al., 2015), forming fractures similar to those formed during the Cretaceous. As the formation time of these fractures was relatively late, the filling degree was lower than that of the Cretaceous fractures, and calcite filling did not form.

6.3. *Petroleum-bearing potential analysis of different fracture stages*

The apertures, distributions, and developing phases of fractures in tight reservoirs affect the migration and accumulation of oil and gas in different ways (Zhang and Lan, 2006; Zeng et al., 2007; Zeng and Li, 2009; Sui, 2015). Previous studies indicate that the Lucaogou Formation entered early oil window maturity in the Late Triassic, with vitrinite reflectance R_o values of 0.5 %. Vitrinite reflectance then reached 0.7 % in the Middle−Late Jurassic, indicating a medium stage of maturity and peak hydrocarbon generation (Fig. 17A). During the formation of the nearly N–S-striking fractures, the Lucaogou Formation had not generated large amounts of petroleum, and the filling degree of the fractures was relatively high; therefore, the petroleum-bearing potential was relatively low. During Stages 2–4, fractures formed from the Middle−Late Jurassic to present-day, which was the peak petroleum generation period of the Lucaogou Formation. These fractures can effectively increase the oil and gas flow under relatively low reservoir porosity and permeability conditions; the petroleum-bearing potential of these fractures is high, and they contain low or no filling, which is more favorable for oil and gas accumulation.

A plan view distribution map of the oil well yields was obtained by analyzing the yields of various production wells in the study area (Fig. 17B). Map shows that the north (with relatively well-developed, nearly N–S-striking fractures) has a relatively low oil well yield, whereas the center and south (with relatively well-developed ENE-striking and WNW-striking fractures) have relatively high oil well yields. However, the developmental degree of the fractures does not show a linear correlation with the oil and gas yield. This result further implies that the nearly N–S-striking fractures are not closely related to the oil and gas migration and accumulation, unlike the late-stage WNW- and ENE-striking fractures.

The research conducted on the petroleum-bearing potential of fractures shows that the central-southern sag is a favorable area for the next stage of exploration. The central-southern area, near the southern Bogda Mountains, has relatively well-developmental fractures. The timing of uplift of the Bogda Mountains was late; therefore, the filing degree of the fractures is low, and the area near the basin sedimentary center was within the oil generation window. These conditions are extremely favorable for the migration and accumulation of the earlier generated oil and gas resources and for the subsequent fracturing. In addition, the former stage of development shows that the central-southern area of the sag contributed most to production, proving that this area has good exploration prospects. Furthermore, organic inclusions are mainly present in the calcite fillings of the later three stages of fracturing, further proving that oil and gas charging began during the formation the Stage 2 fractures (Middle−Late Jurassic).

7. Conclusions

Outcrop, core, microscopic and image log observations demonstrate that tectonic fractures are generally well developed in the Lucaogou Formation and can be basically divided into inclined fractures and bedding-parallel fractures.

According to the crosscutting relations of the fractures from the core observations, AE experiments, C and O stable isotope analyses, Ir analyses, and fluid inclusion temperature measurements, in combination with the knowledge of the tectonic setting and burial history, four fracture developing stages are identified in the tight reservoirs of the Jimsar Sag. During Stage 1, intense N–S compression occurred under a continuous extensional tectonic regime at the end of Late Triassic, which produced many N–S-striking extension fractures. During Stage 2, in

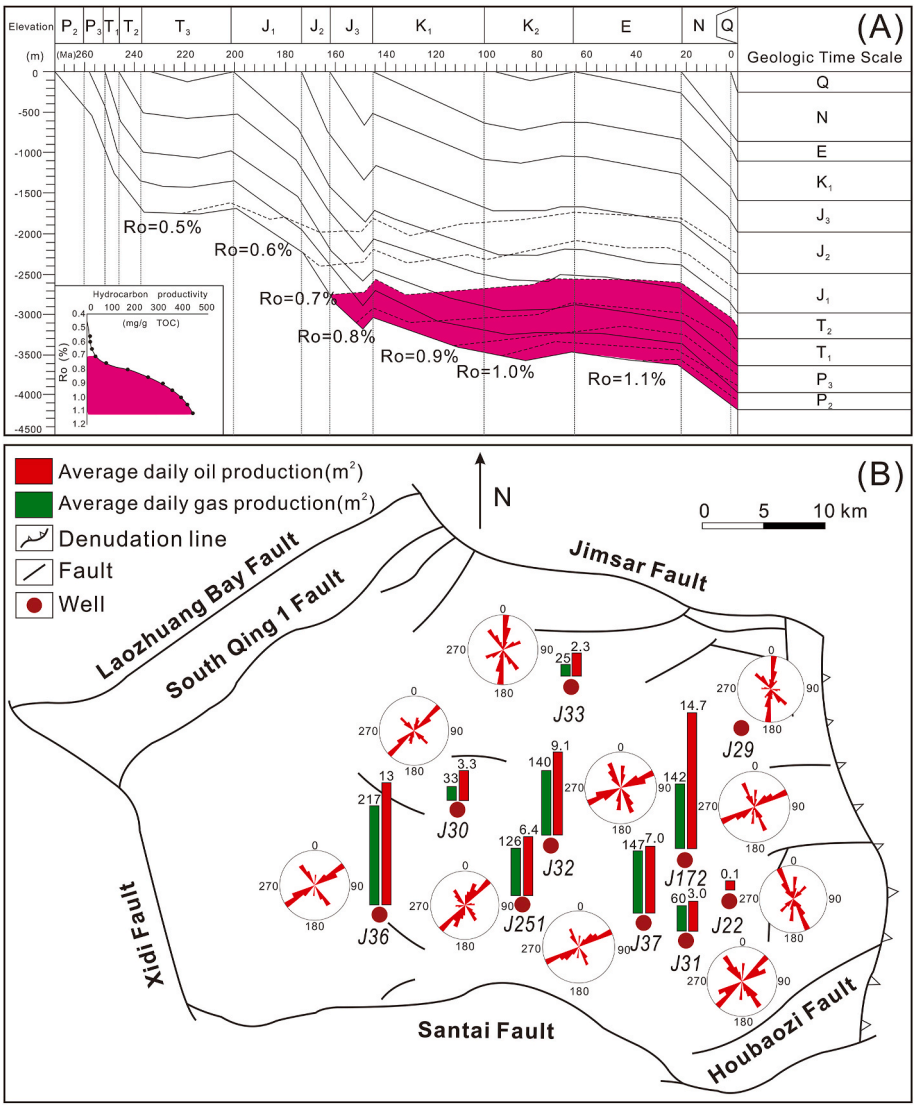

Fig. 17. (A) Burial history and hydrocarbon generation history showing petroleum system elements of the Lucaogou Formation in the Jimusar Sag (modified from Qiu et al., 2016); (B) Congruent map of production and fracture strike in Jimusar Sag.

Middle–Late Jurassic, tectonism in the Tianshan Mountain area was very active, generating NE-trending compressive stress within the basin, forming ENE-striking shear fractures. Stage 3 occurred during the Early Cretaceous; the Bogda piedmont foreland sag experienced continuous folding, which generated intense N–S compressive nappe features within the basin and WNW-striking shear fractures. Stage 4 corresponds to the nearly N–S-trending compressive stress produced by tectonism that has occurred from the Tertiary to the present day; during this stage, WNW-striking shear fractures formed and generally were not filled.

Comparing the timing of the oil generation windows and stages of fracture development, the Stage 1 fractures of the Lucaogou Formation formed early, were highly filled and have a low hydrocarbon-bearing potential. However, the latter three stages have lesser amounts of infill, which favors oil/gas mobility and accumulation and is favorable for oil and gas development within the study area.

Credit author statement

Xiangye Kong: Conceptualization, Methodology, Writing - Original Draft. **Jianhui Zeng:** Data curation, Supervision. **Xianfeng Tan:** Supervision. **Kun Ding:** Formal analysis. **Qun Luo:** Investigation. **Qianyou Wang:** Validation. **Ming Wen:** Resources. **Xin Wang:** Software. **Maoyun Wang:** Software.

Declaration of competing interest

The authors declare that they have no known competing financial interests or personal relationships that could have appeared to influence the work reported in this paper.

Acknowledgements

This work was funded by National Natural Science Foundation of China (Grant No. 41502209 and 41728004), National Key R&D Program of China (Grant No. 2015CB250901) and National Science and Technology Major Project (No. 2016ZX05034-001, 2017ZX05035-002).

Appendix A. Supplementary data

Supplementary data to this article can be found online at https://doi.org/10.1016/j.marpetgeo.2021.105269.

References

Abbasi, M.A., Ezulike, D.O., Dehghanpour, H., Hawkes, R.V., 2014. A comparative study of flowback rate and pressure transient behavior in multifractured horizontal wells completed in tight gas and oil reservoirs. J. Nat. Gas Sci. Eng. 17, 82–93.

Aguilera, R., 1976. Analysis of naturally fractured reservoirs from conventional well logs. J. Petrol. Technol. 28 (7), 764–772.

Becker, S.P., Eichhubl, P., Laubach, S.E., Reed, R.M., Lander, R.H., Bodnar, R.J., 2010. A 48 my history of fracture opening, temperature, and fluid pressure: Cretaceous Travis Peak Formation, East Texas basin. Geol. Soc. Am. Bull. 122 (7–8), 1081–1093.

Bodnar, R.J., 1993. Revised equation and table for determining the freezing point depression of H_2O-NaCl solutions. Geochem. Cosmochim. Acta 57 (3), 683–684.

Cao, Y.C., 2005. Sedimentation and its forming mechanism of the forced lacustrine regression in the rift lacustrine basin. Acta Sedimentol. Sin. 23 (1), 84–90.

Cao, J., Hu, W.X., Yao, S.P., Zhang, Y.J., Wang, X.L., Zhang, Y.Q., Tang, Y., 2006. Evolution of petroleum migration and accumulation in the northwestern margin of the Junggar basin, fluid inclusion geochemistry. Geol. Rev. 52 (5), 700–707.

Cao, Z., Jiang, H., Zeng, J., Saibi, H., Lu, T., Xie, X., Guo, J., 2021. Nanoscale liquid hydrocarbon adsorption on clay minerals: A molecular dynamics simulation of shale oils. Chem. Eng. J. 420, 127578.

Cao, Z., Liu, G., Kong, Y., Wang, C., Niu, Z., Zhang, J., Wei, Z., 2016. Lacustrine tight oil accumulation characteristics: Permian Lucaogou formation in Jimusaer sag, Junggar Basin. Int. J. Coal Geol. 153, 37–51.

Carroll, A.R., Bohacs, K.M., 2001. Lake-type controls on petroleum source rock potential in nonmarine basins. AAPG Bull. 85 (6), 1033–1053.

Chen, J., Deng, C., Liang, D., Wang, X., Zhong, N., Song, F., Xiang, S., 2003. Mixed oils derived from multiple source rocks in the Cainan oilfield, Junggar Basin, Northwest China. Part II: artificial mixing experiments on typical crude oils and quantitative oil-source correlation. Org. Geochem. 34 (7), 911–930.

Clarkson, C.R., Freeman, M., He, L., Agamalian, M., Melnichenko, Y.B., Mastalerz, M., Blach, T.P., 2012. Characterization of tight gas reservoir pore structure using USANS/SANS and gas adsorption analysis. Fuel 95, 371–385.

Cumella, S.P., Scheevel, J., 2008. The Influence of Stratigraphy and Rock Mechanics on Mesaverde Gas Distribution. Piceance Basin, Colorado.

Dong, D.W., Li, L., Wang, X.L., Zhao, L., 2015. Stuctural evolution and dislocation mechanism of western margin Chepaize Uplift of Junggar Basin. J. Jilin Univ. (Earth Sci. Ed.) 45 (4), 1133–1147.

Du, J.H., He, L., Ma, D.S., Fu, J.H., Wang, Y.H., Zhou, T.Y., 2014. Discussion on effective development techniques for continental tight oil in China. Petrol. Explor. Dev. 41 (2), 217–224.

Dutton, S.P., Hamlin, H.S., 1991. Geologic controls on reservoir properties of frontier formation low-permeability gas reservoirs, moxa arch, Wyoming. Low Permeability Reservoirs Symposium. Society of Petroleum Engineers, pp. 479–488.

Epstein, S., Mayeda, T., 1953. Variation of O^{18} content of waters from natural sources. Geochem. Cosmochim. Acta 4 (5), 213–224.

Filho, J.S.D.A., Sepehrnoori, K., 2017. Simulation of planar hydraulic fractures with variable conductivity using the embedded discrete fracture model. J. Petrol. Sci. Eng. 153, 212–222.

Gale, J.F., Laubach, S.E., Olson, J.E., Eichhubl, P., Fall, A., 2014. Natural fractures in shale: a review and new observationsNatural fractures in shale: a review and new observations. AAPG Bull. 98 (11), 2165–2216.

Ge, J.W., Qin, C.G., Zhu, X.M., 2014. Characteristics and origin of low porosity and low permeability sandstone reservoir of Wenchang Formation in HZ25-7 structural belt of Huizhou Depression. Lithologic Reservoirs 26 (4), 36–43.

Gieskes, J., Mahn, C., Day, S., Martin, J.B., Greinert, J., Rathburn, T., McAdoo, B., 2005. A study of the chemistry of pore fluids and authigenic carbonates in methane seep environments: kodiak Trench, Hydrate Ridge, Monterey Bay, and Eel River Basin. Chem. Geol. 220 (3–4), 329–345.

He, D.F., Li, D., Fan, C., Yang, X.F., 2013. Geochronology, geochemistry and tectonostratigraphy of carboniferous strata of the deepest well moshen-1 in the Junggar basin, northwest China: insights into the continental growth of central asia. Gondwana Res. 24 (2), 560–577.

Hennings, P.H., Olson, J.E., Thompson, L.B., 2000. Combining outcrop data and three-dimensional structural models to characterize fractured reservoirs: an example from Wyoming. AAPG Bull. 84 (6), 830–849.

Hu, Q.Y., Dong, D.W., Zhao, L., Li, L., Li, X., Kong, X., 2016. Tectonic evolutionary characteristics and their causes of chepaizi uplift in Junggar basin. Oil Gas Geol. 37 (4), 556–564.

Huang, B., Fu, D., Kusky, T., Ruan, K., Zhou, W., Zhang, X., 2018. Sedimentary provenance in response to carboniferous arc-basin evolution of east junggar and north tianshan belts in the southwestern central asian orogenic belt. Tectonophysics 722, 324–341.

Ji, D.S., Xu, Y.N., Xiao, L.X., Chen, J., 2017. Structural analysis and balance evolution of qigu anticline in the southern edge of Junggar basin. Xinjiang Geol. 35 (3), 262–266.

Jiang, Y.Q., Liu, Y.Q., Yang, Z., Nan, Y., Wang, R., Zhou, P., Yang, Y.J., Zhou, N.C., 2015. Characteristics and origin of tuff-type tight oil in Jimusaer sag, Junggar Basin, NW China. Petrol. Explor. Dev. 42 (6), 810–818.

Khoshbakht, F., Azizzadeh, M., Memarian, H., Nourozi, G.H., Moallemi, S.A., 2012. Comparison of electrical image log with core in a fractured carbonate reservoir. J. Petrol. Sci. Eng. 86, 289–296.

Kong, X.Y., Zeng, J.H., Tan, X.F., Yuan, H., Liu, D., 2021. Genetic Types and Main Control Factors of Microfractures in Tight Oil Reservoirs of Jimsar Sag. Geofluids 2021.

Kuang, L., Tang, Y., Lei, D.W., Chang, Q.S., Min, O.Y., Hou, L.H., Liu, D.G., 2012. Formation conditions and exploration potential of tight oil in the Permian saline lacustrine dolomitic rock, Junggar Basin, NW China. Petrol. Explor. Dev. 39 (6), 700–711.

Lai, J., Wang, G., Fan, Z., Wang, Z., Chen, J., Zhou, Z., Xiao, C., 2017. Fracture detection in oil-based drilling mud using a combination of borehole image and sonic logs. Mar. Petrol. Geol. 84, 195–214.

Laubach, S.E., 1988. Subsurface fractures and their relationship to stress history in East Texas Basin sandstone. Tectonophysics 156 (1–2), 37–49.

Laubach, S.E., 2003. Practical approaches to identifying sealed and open fractures. AAPG Bull. 87 (4), 561–579.

Laubach, S.E., Diaz-Tushman, K., 2009. Laurentian palaeostress trajectories and ephemeral fracture permeability, cambrian eriboll formation sandstones west of the moine thrust zone, NW scotland. J. Geol. Soc. 166 (2), 349–362.

Li, J., Cao, L., Guo, B., Zhang, X., 2017. Prediction of productivity of high energy gas-fractured oil wells. J. Petrol. Sci. Eng. 160, 510–518.

Liang, P., Chen, H., Hollings, P., Wu, C., Xiao, B., Bao, Z., Xu, D., 2016. Geochronology and geochemistry of igneous rocks from the Laoshankou district, North Xinjiang: implications for the late Paleozoic tectonic evolution and metallogenesis of East Junggar. Lithos 266–267, 115–132.

Liu, D., Zhang, C., Yao, E., Song, Y., Jiang, Z., Luo, Q., 2017. What generated the Late Permian to Triassic unconformities in the southern Junggar Basin and western Turpan Basin; tectonic uplift, or increasing aridity. Palaeogeogr. Palaeoclimatol. Palaeoecol. 468, 1–17.

Liu, D., Kong, X., Zhang, C., Wang, J., Yang, D., Liu, X., Song, Y., 2018. Provenance and geochemistry of Lower to Middle Permian strata in the southern Junggar and Turpan basins: a terrestrial record from mid-latitude NE Pangea. Paleogeogr. Paleoclimatol. Paleoecol. 495, 259–277.

Lorenz, J.C., Warpinski, N.R., Branagan, P.T., Settler, A.R., 1989. Fracture characteristics and reservoir behavior of stress-sensitive fracture systems in flat-lying lenticular formations. J. Pet. Sci. Tec. 41 (6), 615–622, 0.

Loyd, S.J., Sample, J., Tripati, R.E., Defliese, W.F., Brooks, K., Hovland, M., Lyons, T., 2016. Methane seep carbonates yield clumped isotope signatures out of equilibrium with formation temperatures. Nat. Commun. 7 (12274).

Lyu, W., Zeng, L., Liu, Z., Liu, G., Zu, K., 2016. Fracture responses of conventional logs in tight-oil sandstones: a case study of the Upper Triassic Yanchang Formation in southwest Ordos Basin, China. AAPG Bull. 100 (9), 1399–1417.

Ma, D., He, D., Li, D., Tang, J., Liu, Z., 2015. Kinematics of syn-tectonic unconformities and implications for the tectonic evolution of the hala'alat Mountains at the northwestern margin of the Junggar basin, central asian orogenic belt. Geosci. Front. 6 (2), 247–264.

Naehr, T.H., Eichhubl, P., Orphan, V.J., Hovland, M., Paull, C.K., Ussler III, W., Greene, H.G., 2007. Authigenic carbonate formation at hydrocarbon seeps in continental margin sediments: a comparative study: deep Sea Research Part II. Topical Studies in Oceanography 54 (11–13), 1268–1291.

Nojabaei, B., Johns, R.T., Chu, L., 2013. Effect of capillary pressure on phase behavior in tight rocks and shales. SPE Reservoir Eval. Eng. 16 (3), 281–289.

Olson, J.E., Taleghani, A.D., 2009. Modeling simultaneous growth of multiple hydraulic fractures and their interaction with natural fractures. In SPE hydraulic fracturing technology conference. Society of Petroleum Engineers.

Pan, S., Horsfield, B., Zou, C., Yang, Z., 2016. Upper Permian Junggar and Upper Triassic Ordos lacustrine source rocks in Northwest and Central China: organic geochemistry, petroleum potential and predicted organofacies. Int. J. Coal Geol. 158, 90–106.

Paul, S.C., Pirskawetz, S., Van Zijl, G.P.A.G., Schmidt, W., 2015. Acoustic emission for characterising the crack propagation in strain-hardening cement-based composites (SHCC). Cement Concr. Res. 69, 19–24.

Pearce, M.A., Jones, R.R., Smith, S.A., McCaffrey, K.J., 2011. Quantification of fold curvature and fracturing using terrestrial laser scanning. AAPG Bull. 95 (5), 771–794.

Pearson, D.G., Woodland, S.J., 2000. Solvent extraction/anion exchange separation and determination of PGEs (Os, Ir, Pt, Pd, Ru) and Re–Os isotopes in geological samples by isotope dilution ICP-MS. Chem. Geol. 165 (1–2), 87–107.

Perez, R.J., Boles, J.R., 2005. Interpreting fracture development from diagenetic mineralogy and thermoelastic contraction modeling. Tectonophysics 400 (1–4), 179–207.

Qiu, Z., Shi, Z.S., Dong, D.Z., Lu, B., Zhang, C.C., Zhou, J., Guo, H.K., 2016. Geological characteristics of source rock and reservoir of tight oil and its accumulation mechanism. A case study of Permian Lucaogou Formation in Jimusar sag, Junggar Basin. Petrol. Explor. Dev. 43 (6), 1013–1024.

Rich, J., Ammerman, M., 2010. Unconventional Geophysics for Unconventional Plays. In SPE Unconventional Gas Conference.

Shinotsuka, K., Suzuki, K., 2007. Simultaneous determination of platinum group elements and rhenium in rock samples using isotope dilution inductively coupled plasma mass spectrometry after cation exchange separation followed by solvent extraction. Anal. Chim. Acta 603 (2), 129–139.

Si, C., Chen, N., Yu, C., Li, Y.W., Meng, X.C., 2013. Sedimentary characteristics of tight oil reservoir in permian Lucaogou Formation, jimsar sag. Petroleum Geology & Experiment 35 (5), 528–533.

Singh, H., Cai, J., 2018. Screening improved recovery methods in tight-oil formations by injecting and producing through fractures. Int. J. Heat Mass Tran. 116, 977–993.

Sonnenberg, S.A., Pramudito, A., 2009. Petroleum geology of the giant elm coulee field, williston basin. AAPG Bull. 93 (9), 1127–1153.

Sui, F., 2015. Tectonic evolution and its relationship with hydrocarbon accumulation in the northwest margin of Junggar basin. Acta Geologica Sinica, v 89 (4), 779–793.

Sun, M., Long, X., Cai, K., Jiang, Y., Wang, B., Yuan, C., Wu, F., 2009. Early Paleozoic ridge subduction in the Chinese Altai: insight from the abrupt change in zircon Hf isotopic compositions. Sci. China Earth Sci. 52 (9), 1345–1358.

Tang, J., Zhang, C.G., Xin, Y., 2017. A fracture evaluation by acoustic logging technology in oil-based mud: a case from tight sandstone reservoirs in Keshen area of Kuqa Depression, Tarim Basin, NW China. Petrol. Explor. Dev. 44 (3), 418–427.

Tao, S., Shan, Y., Tang, D., Xu, H., Li, S., Cui, Y., 2016. Mineralogy, major and trace element geochemistry of Shichanggou oil shales, Jimusaer, Southern Junggar Basin, China: implications for provenance, palaeoenvironment and tectonic setting. J. Petrol. Sci. Eng. 146, 432–445.

Van Golf-Racht, T.D., 1982. Fundamentals of fractured reservoir engineering. Elsevier Science and Technology 12.

Wang, J., Cui, Y.Q., Shi, J.X., Liu, G.P., Xiao, Y., Zeng, L.B., 2016a. Logging response and parameters reconstruction of coal reservoir fractures in the southern Qinshui Basin. Natural Gas Geoscience 27 (11), 2086–2092.

Wang, R.Y., Ding, W.L., Zhang, Y.Q., 2016b. Analysis of developmental characteristics and dominant factors of fractures in Lower Cambrian marine shale reservoirs: a case study of Niutitang formation in Cen'gong block, southern China. J. Petrol. Sci. Eng. 138, 31–49. https://doi.org/10.1016/j.petrol.2015.12.004.

Wang, R.Y., Hu, Z.Q., Sun, C.X., 2018. Comparative analysis of shale reservoir characteristics in the Wufeng-Longmaxi (O3w-S1l) and Niutitang (Є1n) Formations: a case study of the Wells JY1 and TX1 in southeastern Sichuan Basin and its periphery, SW China. Interpretation 6 (4), 31–45. https://doi.org/10.1190/int-2018-0024.1.

Wu, H., Hu, W., Cao, J., Wang, X., Wang, X., Liao, Z., 2016. A unique lacustrine mixed dolomitic-clastic sequence for tight oil reservoir within the middle Permian Lucaogou Formation of the Junggar Basin, NW China: reservoir characteristics and origin. Mar. Petrol. Geol. 76, 115–132.

Xi, K.L., Cao, Y.C., Zhu, R.K., Shao, Y., Xue, X.J., Wang, X.J., Zhang, J., 2015. Rock types and characteristics of tight oil reservoir in Permian Lucaogou Formation, Jimsar sag. Acta Pet. Sin. 36 (12), 1495–1507.

Xiao, F.F., Hou, G.T., Li, J.H., 2010. Controlling of Cenozoic structural stress to the development of fractures in Carboniferous volcanic rocks, Junggar Basin. Acta Petrol. Sin. 26 (1), 255–262.

Xiao, X.L., Jin, X.J., Zhang, X., 2015. Fracture identification based on information fusion of conventional logging and electrical imaging logging. Oil Geophys. Prospect. 50 (3), 542–547.

Xie, X., Borjigin, T., Zhang, Q., Zhang, Z., Qin, J., Bian, L., Volkman, J.K., 2015. Intact microbial fossils in the Permian Lucaogou Formation oil shale, Junggar basin, NW China. Int. J. Coal Geol. 146, 166–178.

Yang, H.B., Chen, L., Kong, Y.H., 2004. A novel classification of structural units in Junggar Basin. Xinjing Pet. Geol. 25 (6), 686–688.

Yi, Z., Huang, B., Xiao, W., Yang, L., Qiao, Q., 2015. Paleomagnetic study of late paleozoic rocks in the tacheng basin of west junggar (NW China): implications for the tectonic evolution of the western altaids. Gondwana Res. 27 (2), 862–877.

Zazoun, R.S., 2013. Fracture density estimation from core and conventional well logs data using artificial neural networks: the Cambro-Ordovician reservoir of Mesdar oil field, Algeria. J. Afr. Earth Sci. 83, 55–73.

Zeng, L.B., Li, X.Y., 2009. Fractures in sandstone reservoirs with ultra-low permeability: a case study of the upper triassic yanchang formation in the ordos basin, China. AAPG Bull. 93 (4), 461–477.

Zeng, L.B., Shi, C.G., Wang, Y.K., Li, S.H., Wan, X.L., Cui, P.F., 2007. The pressure sensitivity of fractures and its development significance for extra lowpermeability sandstone reservoirs in Ordos Basin. Eng. Sci. 9, 35–38.

Zeng, L.B., Ke, S.Z., Liu, Y., 2010. Fracture Study Methods for Low Permeability Oil and Gas Reservoir. Petroleum Industry Press, Beijing, p. 187.

Zeng, L.B., Su, H., Tang, X., Peng, Y., Gong, L., 2013. Fractured tight sandstone oil and gas reservoirs: a new play type in the Dongpu depression, Bohai Bay Basin, China. AAPG Bull. 97 (3), 363–377.

Zhang, J.F., Lan, C.L., 2006. Fractures and faults distribution and its effect on gas enrichment areas in Ordos Basin. Petrol. Explor. Dev. 33 (2), 172.

Zhang, M.L., Wan, Y.X., Xie, F.L., 2014. Technology and practice of increasing drilling rate for tight oil in Jimusar. Oil Drilling & Production Technology 36 (5), 18–21.

Zhang, K., Jia, C.Z., Yan, S., 2020a. Analysis of Lower Cambrian shale gas composition, source and accumulation pattern in different tectonic backgrounds: a case study of Weiyuan Block in the Upper Yangtze region and Xiuwu Basin in the Lower Yangtze region. Fuel 263, 115978.

Zhang, K., Peng, J., Liu, W.W., 2020b. The role of deep geofluids in the enrichment of sedimentary organic matter: a case study of the Late Ordovician-Early Silurian in the upper Yangtze region and early Cambrian in the lower Yangtze region, south China. Geofluids 2020, 8868638.

Zhang, K., Peng, J., Wang, X., 2020c. Effect of organic maturity on shale gas genesis and pores development: a case study on marine shale in the upper Yangtze region, South China. Open Geosci. 12, 1617–1629.

Zhang, C., Zhu, D., Luo, Q., Liu, L., Liu, D., Yan, L., 2017. Major factors controlling fracture development in the Middle Permian Lucaogou Formation tight oil reservoir, Junggar Basin, NW China. Journal of Asian Earth Sciences 146, 279–295.

Zhao, B., 1992a. Formation and evolution of Junggar basin. Xinjing Pet. Geol. 133, 191–196.

Zhao, B., 1992b. Nature of basement of Junggar basin. Xinjing Pet. Geol. 132, 95–99.

Zhao, Z., Du, J., 2012. Tight Oil and Gas. Petroleum Industry Press, Beijing, pp. 1–199.

Zhao, S., Li, S., Liu, X., Suo, Y., Dai, L., Lou, D., Yang, Z., 2014. Intracontinental orogenic transition: insights from structures of the eastern Junggar basin between the altay and tianshan orogens. J. Asian Earth Sci. 88, 137–148.

Zhu, W., Wu, C.D., Wang, J., 2017. Triassic provenance and its tectonic significance in sikeshu sag, Junggar basin. Xinjing Pet. Geol. 38 (5), 513–518.

Zou, C.N., Zhu, R.K., Wu, S.T., Yang, Z., Tao, S.Z., Yuan, X.J., Bai, B., 2012. Types, characteristics, genesis and prospects of conventional and unconventional hydrocarbon accumulations: taking tight oil and tight gas in China as an instance. Acta Pet. Sin. 33 (2), 173–187.